BMC Chemistry

RESEARCH

Open Access

Synthesis of thiazoloquinolinone derivatives: molecular docking, MD simulation, and pharmacological evaluation as VEGFR-2 inhibitors

Zeinab Amiri[1], Mohammad Bayat[1*] and Davood Gheidari[2*]

Abstract

We synthesized a series of novel thiazoloquinolinone derivatives, achieving moderate to high yields ranging from 74 to 96%, and assessed their efficacy against Vascular Endothelial Growth Factor Receptor-2 (VEGFR-2) using in silico methodologies. The structures of these compounds were characterized through various spectroscopic techniques, including ^{1}H-NMR, ^{13}C-NMR, IR, and mass spectrometry. Comprehensive computational analyses, encompassing molecular docking, molecular dynamics (MD) simulations, and absorption, distribution, metabolism, excretion, and toxicity (ADMET) profiling, were conducted. Docking studies with VEGFR-2 revealed that all synthesized compounds exhibited docking scores between − 3.24 and − 6.63, indicating varying degrees of binding affinity. Notably, compound **(5e)** demonstrated the strongest binding affinity with an energy of − 6.63 kcal/mol. The MD simulations indicated that Lys868 was one of the amino acids exhibiting the highest frequency of interaction throughout the simulation. Analysis of the ADMET and physicochemical properties revealed that all inhibitor compounds possess favorable pharmacological characteristics.

Keywords Thiazoloquinolinone, VEGFR-2 inhibitors, MD simulation, Pharmacological evaluation

Introduction

According to estimates from the World Health Organization (WHO), cancer is the second leading cause of mortality in approximately 112 countries, while it ranks as the third or fourth leading cause in around 23 other nations. Projections indicate that the global incidence of new cancer cases will reach nearly 28 million by 2040 [1]. Significant efforts have focused on developing effective and low-toxicity anticancer agents in response to this increasing burden [2]. A hallmark of many cancer types is the upregulation of angiogenesis, a critical process for tumor growth. Activation of several chemical signaling pathways drives angiogenesis, the development of new blood vessels from pre-existing vasculature [3]. Many cancer cells overexpress their receptors, including VEGFR-2, which is crucial in the control of tumor angiogenesis [4]. Upon activation, VEGFR-2 initiates a series of signals that support cell survival, growth, and proliferation [4]. Cancer cells display hyperactive VEGFR-2 receptors compared to normal cells. This finding allows researchers to target these receptors therapeutically to create safe and selective drugs that inhibit angiogenesis in cancer cells without affecting normal cells. According to the literature, VEGFR-2 inhibitors possess four key

*Correspondence:
Mohammad Bayat
bayat_mo@yahoo.com
Davood Gheidari
davoodgheidari@gmail.com; davoodgheidari@phd.guilan.ac.ir
[1] Department of Chemistry, Faculty of Science, Imam Khomeini International University, Qazvin, Iran
[2] Department of Chemistry, Faculty of Science, University of Guilan, Rasht, Iran

pharmacophoric features: (i) a heteroaromatic ring structure capable of engaging at the hinge region [5]; (ii) a spacer moiety that can be directed in the spacer region of the active sites [6]; (iii) a pharmacophore moiety, such as an amide or urea, that can bind at the DFG motif region; and (iv) a hydrophobic group that resides in the allosteric pocket of the VEGFR-2 binding site [7]. Sorafenib [8] is a synthetic compound, specifically a picolinamide and phenylurea derivative, that targets growth signaling pathways and angiogenesis by inhibiting the VEGFR-2 signaling cascade, thereby suppressing tumor angiogenesis. It exhibits a typical pharmacophoric structure with an aryl ring in the center connected to a pyridine ring by an ether bond, which serves as the head group, and a urea moiety that connects the two rings at their ends [9]. Pazopanib [10] is another inhibitor of VEGFR-2, distinguished by several important characteristics. The presence of aromatic ring structures promotes π-π stacking interactions with amino acids located within the binding site, thereby increasing binding affinity. Furthermore, a pyrimidine moiety derived from quinoxaline occupies the gatekeeper region, serving as a central aromatic linker that contributes to the compound's structural integrity and binding efficacy. Additionally, hydrophobic regions contribute to van der Waals interactions, which are essential for receptor affinity. Despite its high efficacy and selectivity, sorafenib is associated with many side effects. Similarly, various toxicities of pazopanib have been reported, including depigmentation phenomena, proteinuria, hepatotoxicity, hypothyroidism, as well as hypertension, thrombosis, and cardiac dysfunction [11]. In light of the side effects associated with compounds such as sorafenib and pazopanib, researchers are actively engaged in the design of novel compounds through the strategy of molecular hybridization. This methodology facilitates the integration of advantageous properties from multiple compounds, aiming to mitigate side effects while preserving therapeutic efficacy and selectivity. By optimizing these attributes in the development of new compounds, scientists seek to minimize undesirable effects while enhancing overall therapeutic performance, potentially leading to innovative pharmaceuticals that demonstrate improved anti-cancer activity with fewer side effects. Among the promising candidates in this context are heterocyclic compounds, which are organic molecules containing one or more heteroatoms within their ring structures. These compounds are significant in medicinal chemistry due to their diverse biological activities and are frequently employed as scaffolds in drug design. Notably, compounds featuring thiazole rings are recognized as important chemical scaffolds [12], often referred to as privileged pharmacophores due to their ability to interact readily with a broad spectrum of biological targets. Thiazole derivatives have exhibited a wide array of biological activities, including anticancer, antimicrobial, and anti-inflammatory effects [13–15], thereby attracting considerable research interest. In 2023, El-Hazek et al. [16] synthesized thiazoloquinoxaline as a VEGFR-2 inhibitor. They demonstrated that the quinoxaline ring functions as the heteroaromatic moiety occupying the hinge region, which is anticipated to provide more binding interactions than the pyridine ring of sorafenib and to serve as a bioisostere for the indazole ring of pazopanib. The thiazole ring acts as the central aromatic linker, occupying the gatekeeper region, with the 1,3-substituted ring exhibiting superior activity in VEGFR-2 inhibition, in addition to offering enhanced regioselectivity and stability. The thiazole ring, in conjunction with the central imine, is proposed as a hydrogen bond donor (HBD) and acceptor (HBA) pharmacophore, aimed at forming hydrogen bonds for inhibitory activity against VEGFR-2, thereby resembling the amino pyrimidine ring of pazopanib. Additionally, Tokalı et al. [17] successfully synthesized quinazoline derivatives with novel pharmacophore properties, which contributed to enhanced efficacy as potential VEGFR-2 inhibitors. Through the design of these new pharmacophores, they achieved anti-cancer activity against the A549 lung adenocarcinoma cell line. Dihydrothiazol-4-yl)benzonitrile is another compound that demonstrated strong antitumor activity against the C6 cell line, with an IC_{50} value of 3.83 μM, significantly outperforming cisplatin (IC_{50} = 12.67 μM) as a reference drug [18]. Furthermore, dihydroquinolin-4-yl)piperazin-1-yl)acetamide, which features a 4-chlorophenylthiazole ring, was shown to inhibit VEGFR-2 kinase activity with an IC_{50} value of 51.09 nM, comparable to sorafenib's IC_{50} of 51.41 nM [19]. Another derivative, hydrazineyl thiazole, exhibited promising cytotoxic activity through potent EGFR-TK inhibition [20] (Fig. 1).

In the past decade, molecular docking and MD studies have emerged as pivotal methodologies in drug design and discovery, showcasing their substantial impact on the field. Molecular docking is a computational technique employed to predict the interactions between a specific ligand and its protein target. This approach utilizes computer simulations to identify the parameters that influence the formation and strength of the bonds between the ligand and the receptor. Building on the insights gained from molecular docking, MD studies serve as an in silico method to assess the stability of the ligand–protein complex over time. Furthermore, in silico methods can be utilized to evaluate drug ADMET properties, as well as drug-likeness, to assess the druggability of potential candidates. The discovery of new therapeutic agents often involves determining their biological activities, a process that can be costly, complex, and time-consuming.

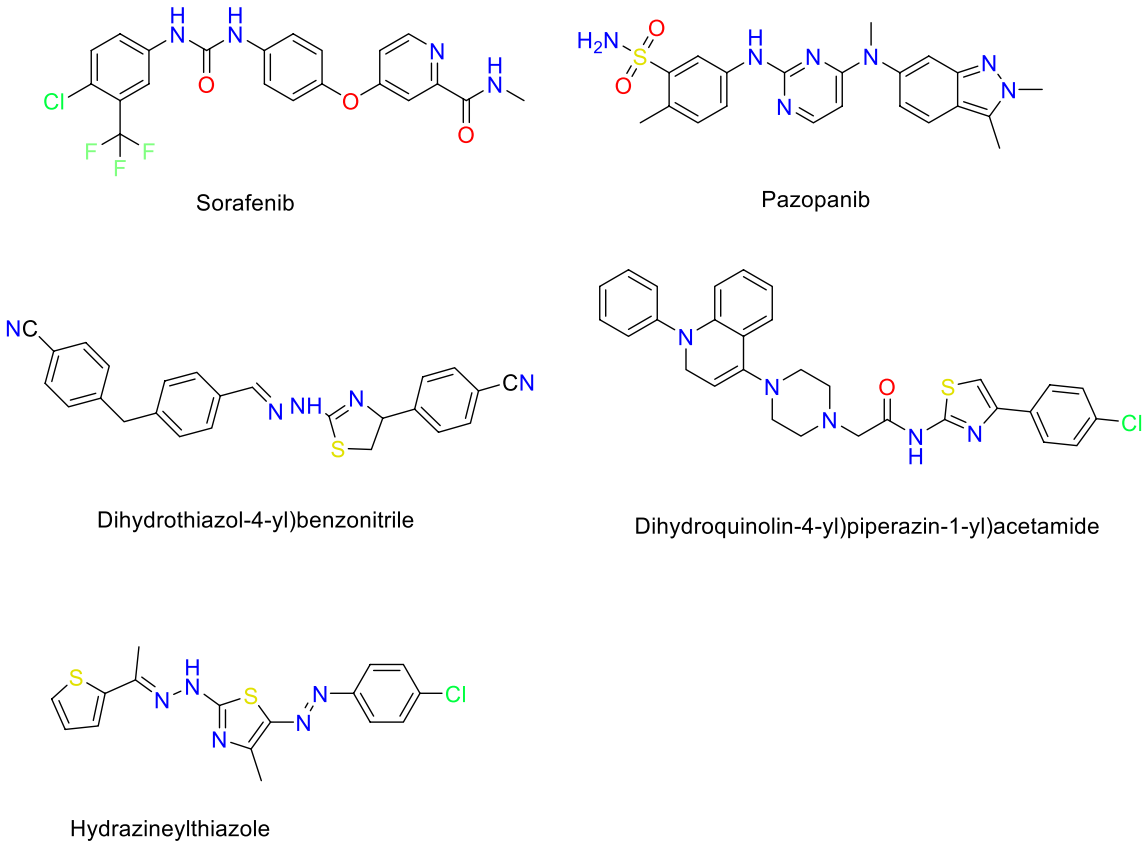

Fig. 1 Chemical structures of sorafenib, pazopanib, and some bioactive thiazole derivatives

Molecular modeling techniques provide valuable insights into the biological activities of novel agents, making them instrumental in identifying promising drug molecules among these candidates [21]. Based on studies of thiazole derivatives and our ongoing research into the synthesis of bioactive heterocyclic compounds [22–26], this study aims to develop a new series of thiazoloquinolines as thiazole derivatives. This is achieved through a one-pot, multicomponent reaction involving 2-(nitromethylene)thiazolidine, which is formed by combining cysteamine hydrochloride with ketene *N*,*S*-acetals, along with aldehydes and cyclohexane-1,3-dione, targeting VEGFR-2 with key pharmacophoric features. The synthesized compounds exhibit several important pharmacophoric characteristics that enhance their potential as drug candidates. Notably, these derivatives contain heteroaromatic ring, which facilitate π–π stacking interactions with target receptors, thereby increasing binding affinity. The presence of a hydroxyl group (–OH) serves as a HBD, while the carbonyl (C=O) and nitro (NO_2) groups act as HBA, further promoting interactions with the receptor. Additionally, the methoxy group ($–OCH_3$) and the aromatic rings contribute to the compounds' lipophilic character, enhancing hydrophobic interactions with the receptor. A central linker connects these pharmacophoric elements, providing flexibility and optimal spatial orientation for binding. Furthermore, the inclusion of a sulfur atom (S) may contribute to specific interactions, potentially enhancing the compounds' biological activity. These features underscore the promising potential of the newly developed thiazoloquinolines as drug candidates targeting VEGFR-2. To further evaluate this potential, we also investigated ligand–protein interactions and assessed the stability of the ligand–protein complexes using molecular docking and MD simulations.

Results and discussion

Chemistry

We have synthesized a straightforward and efficient method for producing thiazoloquinolinone derivatives **(5a–l)** through a four-component reaction. We studied the reaction of thiazoloquinolinone derivatives **(5a–l)** made from ketene acetal **(6)**, aromatic aldehydes **(3)**, and 1,3-cyclohexanone **(4)** under various reaction conditions (Scheme 1).

To achieve optimum conditions, we conducted various experiments with different solvents and catalysts. In ethanol with triethylamine as a catalyst (entry 1,

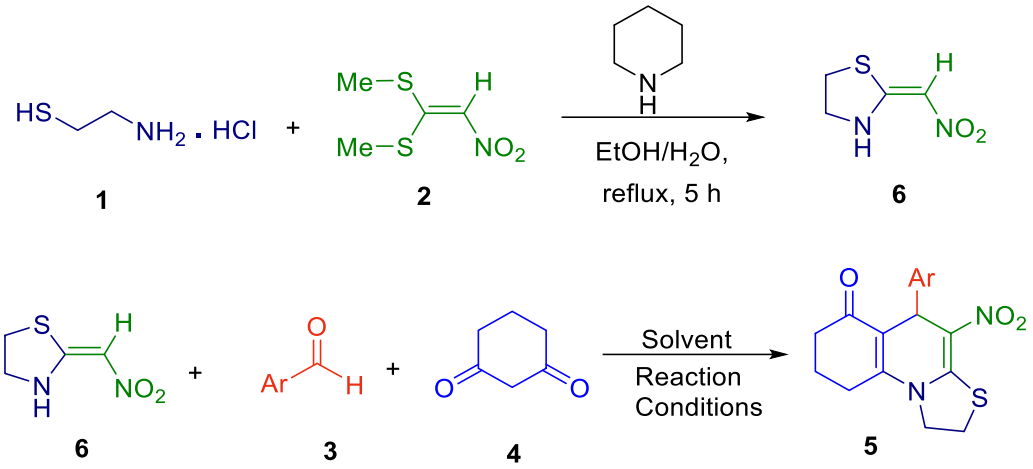

Scheme 1 Synthetic scheme for the products **(5a–l)**

Table 1 Optimize reaction conditions for the production of **(5a)**

Entry	Solvent	Temp (°C)	Catalyst (10%)	Time (min)	Yield (%)
1	EtOH	80	Et_3N	35	54
2	MeH	65	Piperidine	20	60
3	H_2O	80	Piperidine	15	65
4	**EtOH/H_2O(1:1)**	**80**	**Piperidine**	**20**	**77**
5	**CH_3CN/H_2O(1:1)**	**80**	**Et_3N**	**240**	**94**
6	EtOH/ H_2O(1:1)	80	Et_3N	45	75

Bold indicates optimum conditions

Table 1), methanol with pyridine as a catalyst (entry 2, Table 1), and water with pyridine as a catalyst (entry 3, Table 1), the reaction times and yields were shorter. We also performed the reaction using different ratios of ethanol/water (entry 4, Table 1) with pyridine, acetonitrile/water (entry 5, Table 1) with triethylamine, and ethanol/water with triethylamine (entry 6, Table 1). Given the environmental parameters and the decreased reaction time, we preferred the conditions of entry 5.

The spectral data of the products are consistent with those reported for similar structures in the literature [27]. The detailed structures of the synthesized derivatives are provided in Table 2. The ^{1}H-NMR spectrum of compound **(5a)** showed multiple signals for the CH_2 and CH_2S groups (δ 3.39–3.43), two multiplets for the CH_2N group (δ 4.20–4.27), a signal for the methine group (δ 5.28 ppm)., and two multiplets for the aromatic region (δ 7.13–7.17, 7.23–7.27 ppm). The ^{13}C-NMR spectrum of product **(5a)** displayed 17 distinct resonances. The IR spectrum of this compound exhibited absorption bands related to C=O stretching (1654 cm^{-1}), as well as bands at 1539, 1370, and 1215 cm^{-1} due to the NO_2 and C–N groups. Additionally, the mass spectrum of **(5a)** showed a molecular ion peak at $m/z = 328$, consistent with the proposed structure.

The ^{13}C NMR spectrum of **5c**, exhibits nineteen distinct signals due to the carbon–fluorine coupling of aryl moeity in the molecule. The *ipso* carbon bearing fluorine atom appears as a doublet at 160.8 ($^1J_{CF} = 181.7$ Hz), *ortho* carbons appear as a doublet at 114.7 ($^2J_{CF} = 15.8$ Hz), *meta* carbons appear as a doublet at 129.7 (*d*, $^3J_{CF} = 6.8$ Hz), and *para* carbon appears as a doublet at 139.9 (*d*, $^4J_{CF} = 2.2$ Hz). The detailed structures of the synthesized derivatives are provided in Fig. 2.

Scheme 2 illustrates a proposed mechanism for the generation of thiazoloquinolinone derivatives **(5a)**. Initially, the interaction of cysteamine hydrochloride **(1)** and ketene *N,S*-acetal **(2)** with piperidine generates 2-(nitromethylene)thiazolidine **(6)**. Then, the condensation of 1,3-cyclohexanedione **(4)** with aldehyde **(3)** results in adduct **(7)**. Subsequently, intermediate **(7)** undergoes Michael addition with 2-(nitromethylene) thiazolidine **(6)** to produce intermediate **(8)**, which then experiences imine-enamine tautomerization. This

Table 2 Molecular structures and percentage yields of compounds **(5a–l)**

Entry	ArCHO	Product	Time (min.)	Yield (%)
1	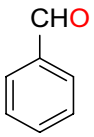	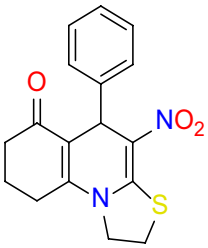	35	96
2	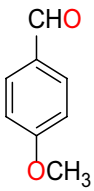	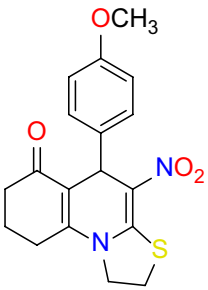	15	83
3	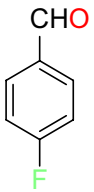	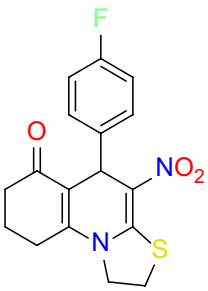	35	81
4	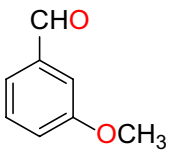	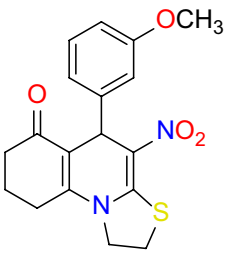	20	80
5	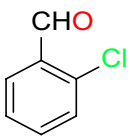	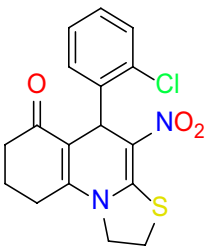	40	74

Table 2 (continued)

Entry	ArCHO	Product	Time (min.)	Yield (%)
6	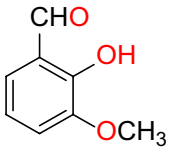	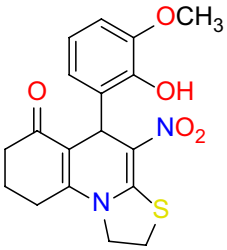	30	90
7	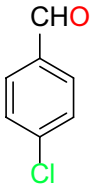	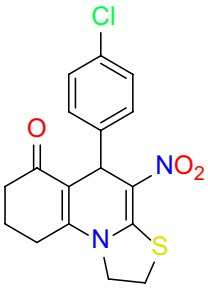	20	77
8	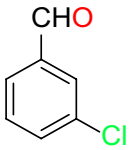	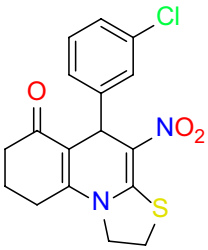	25	82
9	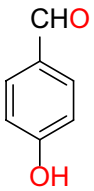	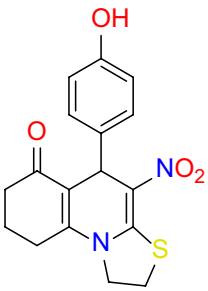	60	89
10	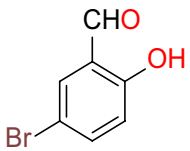	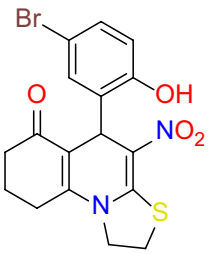	35	76

Table 2 (continued)

Entry	ArCHO	Product	Time (min.)	Yield (%)
11	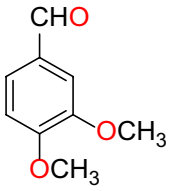	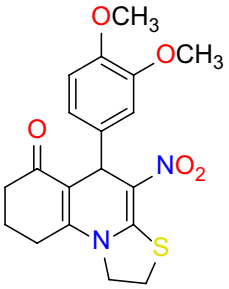	15	80
12	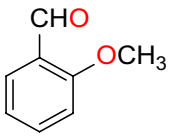	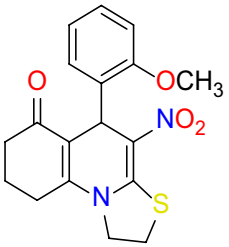	25	76

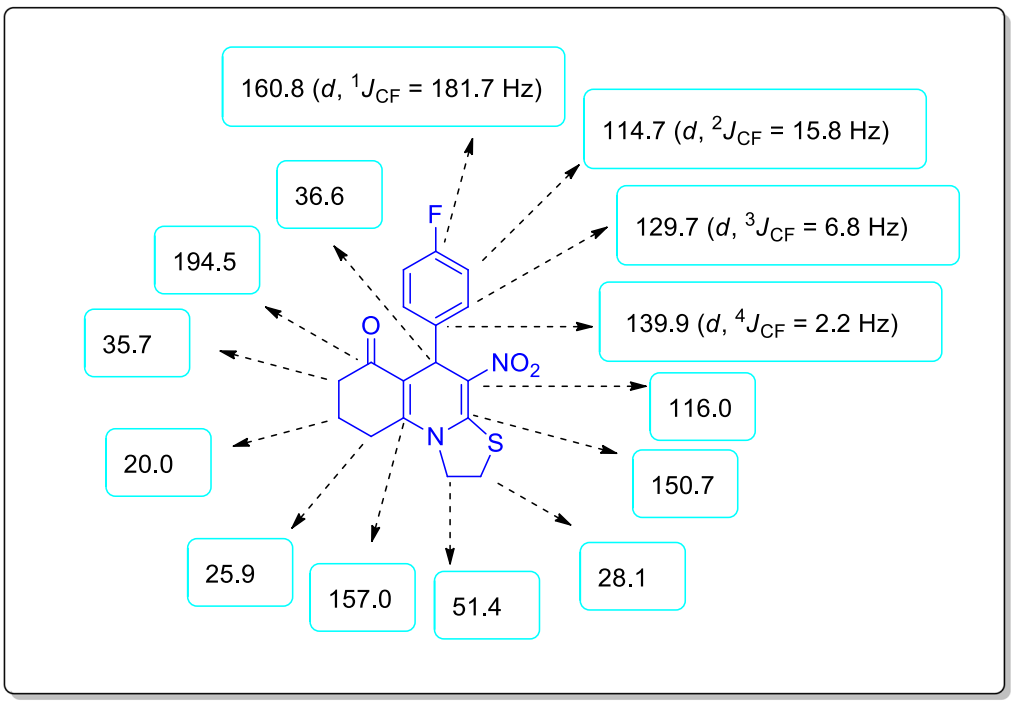

Fig. 2 The ^{13}C chemical shifts of **(5c)**

is followed by the secondary amino group undergoing nucleophilic addition to the C=O group and subsequent cyclization, ultimately resulting in the formation of compound **(5)**.

Computational studies

Docking studies

In *silico* docking studies were conducted to elucidate the key interaction points between the synthesized compounds and the VEGFR-2 binding pocket. These studies

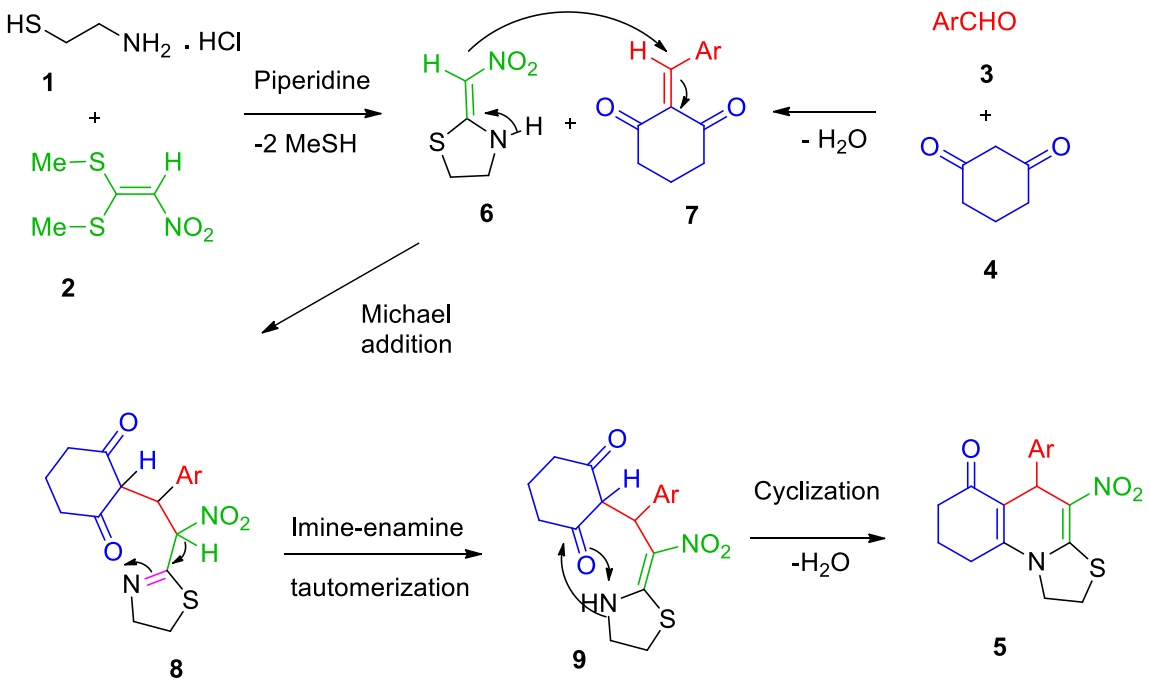

Scheme 2 Proposed mechanism for the production of product **(5)**

are essential for understanding the molecular interactions between the synthesized compounds and the target protein, VEGFR-2, which plays a significant role in angiogenesis and tumor progression. By employing computational docking techniques, we aimed to predict the binding affinities and orientations of the compounds within the VEGFR-2 active site. The docking process involved the preparation of the protein structure and the ligands, followed by the application of an appropriate docking algorithm to simulate the binding interactions. This methodology facilitates the identification of critical amino acid residues involved in the binding process, providing insights into the molecular interactions that contribute to the biological activity of the compounds. The results from these docking studies not only validate the potential efficacy of the synthesized compounds but also inform further optimization of their chemical structures for enhanced binding affinity and specificity. For this purpose, the VEGFR-2 structure (PDB: 2OH4) was selected due to its well-characterized binding pocket and its pivotal role in mediating angiogenic signaling pathways. This specific protein structure serves as a reliable template for understanding how potential therapeutic compounds can interact with VEGFR-2. The Protein Data Bank (PDB) [28] entry 2OH4 contains comprehensive information about the three-dimensional conformation of VEGFR-2, including the arrangement of key amino acid residues involved in ligand binding. To ensure the accuracy and reliability of our docking studies, the docking protocol was validated by re-docking the native ligand BAX into the active site of VEGFR-2. This validation step is critical, as it demonstrates the capability of the docking software to reproduce known binding interactions. The re-docking process successfully replicated the original binding pattern of BAX, achieving a root-mean-square deviation (RMSD) value of 1.01 Å. This low RMSD value indicates a high degree of similarity between the docked conformation and the crystallographic conformation of the ligand, thereby confirming the reliability of the docking procedure [29]. Such validation not only reinforces the credibility of our docking results but also enhances confidence in the predictive power of the computational methods employed in this study (Fig. 3).

After validation, we proceeded to dock all synthesized compounds **(5a–l)** into the VEGFR-2 binding site. As shown in Table 3, several key residues, including Arg1027, Leu889, Asp814, Lys868, Asp1046, Glu885, Ile888, Ile1025, Cys1024, His1026, Ile892, Val899, Cys1045, Gly1048, Ala881, Ser884, Leu1049, Asp1028, Leu1019, Val898, Ile1044, Leu813, Cys817, and Val916, played crucial roles in the binding interactions with the compounds **(5a–l)**. The synthesized compounds had docking scores ranging from − 3.248 to − 6.635 kcal/mol, indicating varying degrees of binding affinity to the VEGFR-2 target. A lower (more negative) docking score suggests a stronger predicted binding affinity.

Compound **(5e)** exhibited the lowest binding free energy of − 6.635 kcal/mol, indicating its strong affinity

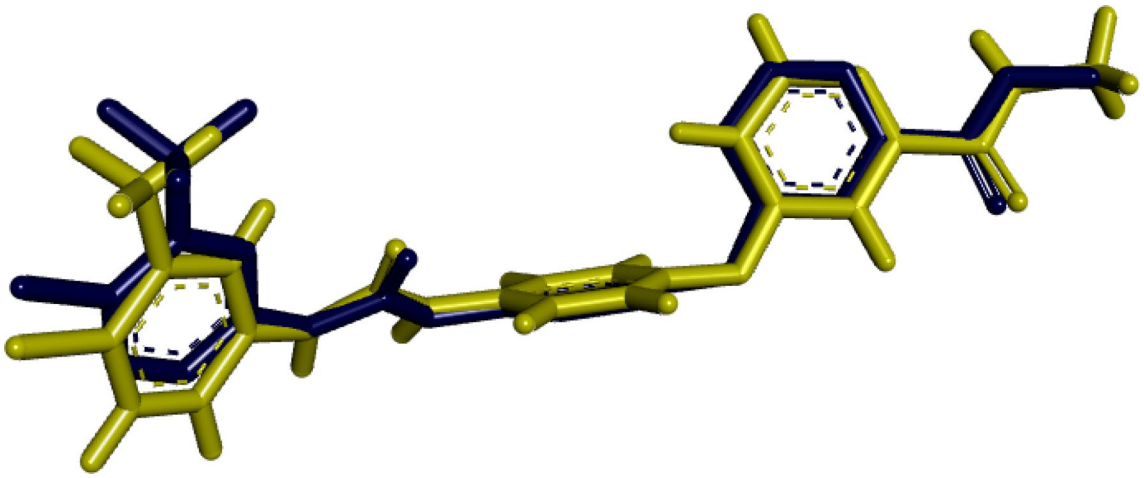

Fig. 3 Superimposition of the co-crystal ligand (blue) and the docked ligand (yellow)

for the target protein. This compound formed a hydrogen bond between its nitro group and the residue Asp1046, characterized by a hydrogen bond length of 3.01 Å. Hydrogen bonds are crucial for stabilizing the interaction between ligands and their target proteins, as they contribute to the specificity and strength of binding. Furthermore, two carbon-hydrogen bond interactions were observed: the first interaction occurred between the hydrogen of thiazolidine and the residue Asp814, with a bond length of 2.63 Å; the second interaction involved the carbonyl group of cyclohex-2-en-1-one and the residue His1026, with a bond length of 2.75 Å. These carbon-hydrogen interactions also play a significant role in the overall binding affinity, as they help to maintain the structural integrity of the complex and facilitate the proper orientation of the ligand within the binding site. Furthermore, two hydrophobic alkyl interactions were detected between the cyclohex-2-en-1-one ring and the residues Cys1024 and Ile888. It demonstrated three charge interactions with the residues Asp1046, Glu885, Lys868, and Ile1044, in addition to seven van der Waals interactions. Figure 4 presents a comprehensive 3D and 2D representation of the interactions of compound **(5e)** inside the active site of VEGFR-2. Conversely, compound **(5b)**, with a docking score of − 3.248 kcal/mol, shows limited interaction with key residues, indicating that modifications to its structure may be necessary to enhance its binding affinity. The presence of multiple key residues across different compounds suggests that a common binding motif may exist, which could be targeted for the design of more potent VEGFR-2 inhibitors. The analysis of interaction residues revealed that several amino acids consistently participate in binding across multiple compounds. Key residues identified as significant contributors to the binding interactions included Arg1027 and Lys868, which were frequently observed in compounds **(5a)**, **(5b)**, **(5d)**, **(5f)**, **(5h)**, **(5i)**, **(5j)**, **(5k)**, and **(5l)**. Their presence suggests they play a crucial role in stabilizing the ligand-receptor complex through hydrogen bonding. Additionally, Asp814 and Glu885 appeared in multiple compounds, indicating their importance in hydrogen bonding, charge interactions, and van der Waals interactions. Furthermore, compounds such as **(5b)**, **(5d)**, **(5f)**, **(5g)**, **(5h)**, **(5k)**, and **(5l)** exhibited significant hydrophobic interactions with residues such as Ala881, contributing to the overall stability of the ligand within the binding pocket. All compounds demonstrated van der Waals interactions with various residues, which are essential for fine-tuning the binding affinity. However, some compounds, such as **(5c)**, and **(5g)**, exhibited unfavorable negative-negative interactions with residues like Asp814, indicating potential steric clashes or repulsive forces that could affect binding efficacy.

MD simulation

RMSD serves as a critical metric in MD simulations, utilized to quantify the structural deviation of biomolecules over time. It measures the mean distance between atoms in a reference structure and their positions at subsequent time points, thereby providing insights into the stability and conformational alterations of proteins and ligands. In the context of protein–ligand interactions, monitoring RMSD facilitates the assessment of the dynamics of binding and unbinding, as well as the overall stability of the complex. Variations in RMSD values indicate conformational adjustments, rendering it an indispensable tool for elucidating binding mechanisms and enhancing drug design. The plot presented in Fig. 5 illustrates the RMSD of both the protein and the ligand over a 100-ns MD simulation.

Table 3 Docking scores, and interactions of each synthesized compound **(5a–l)**

Compound	Docking score (kcal/mol)	Interaction residue						
		Hydrogen bond		Hydrophobic	Charge	Van der walls	Unfavorable negative-negative	Other
		H-bonding	C-bonding					
5a	− 3.974	Arg1027		Leu889	Asp814, Lys868, Asp1046, Glu885	Ile888, Ile1025, Cys1024, His1026, Ile892, Val899, Cys1045, Gly-1048Ala881, Ser884		
5b	− 3.248	Lys868		Ala881, Arg1027	Glu885, Asp1046, Lys868	Leu889, Ile888, Ile1025, His1026, Asp814, Ser884, Leu1049, Gly1048		
5c	− 4.075	Arg1027	Glu885	Leu1049, His1026	Asp1046, Asp814, Glu885	Ser884, Ile888, Ala881, Gly1048, Asp1028, Leu1019, Cys1024, Ile1025, Ile892	Asp814	
5d	− 3.488	Arg1027,Lys868		Leu889, Ala881	Asp814, Lys868, Glu885, Asp1046	Ser884, Ile888, Ile1025, Cys1024, His1026, Ile892, Cys1045, Val899, Gly1048		
5e	− 6.635	Asp1046	Asp814(2.63),His1026(2.75)	Leu1019, Val898, Ile892, Cys1024, Ile888	Asp1046, Glu885, Lys868	Val899, Cys1045, Ile1044, Ile1025, Leu813, Arg1027, Leu889		
5f	− 4.076	Lys868, Asp814	Asp814	Arg1027, Cys817, Ala881	Lys868, Glu885, Asp1046	Ser884, Ile1025, His1026, Leu889, Gly1048, Ile888, Leu1049		
5g	− 4.031	Arg1027	Glu885	Leu1049, Leu1019, Ala881, His1026	Asp814, Glu885	Asp1028, Asp1046, Gly1048, Ile888, Ser884, Ile892, Ile1025, Cys1024	Asp814	Ala881

Table 3 (continued)

Compound	Docking score (kcal/mol)	Interaction residue						
		Hydrogen bond		Hydrophobic	Charge	Van der walls	Unfavorable negative-negative	Other
		H-bonding	C-bonding					
5h	– 4.073	Lys868		Ala881, Ile888, Leu889	Glu885, Lys868, Asp1046, Asp814	Arg1027, Ile1025, Cys1024, His1026, Leu1019, Ile892, Cys1045, Val899, Gly1048, Ser884		Asp1046
5i	– 4.28	Arg1027		Cys1024, Leu1019, Leu889	Lys868, Glu885, Asp1046, Arg1027	Asp1028, His1026, Asp814, Ile888, Ile1025, Ile892, Ile1044, Cys1045, Val899		
5j	– 4.55	Lys868	Asp814	Val899, Val916, Leu889	Lys868, Glu885, Asp1046	Cys1045, Ile1044, Ile888, Leu1019, Ile892, His1026, Cys1024, Ile1025, Arg1027, Gly1048		
5k	– 3.561	Ser884,Lys868	Ser884,Asp814	Arg1027, Ile888, Cys817, Ala881	Lys868, Glu885, Asp1046	Ile1025, His1026, Leu889, Gly1048, Leu1049		
5l	– 3.580	Ser884		Ile888, Ala881	Asp814	Leu889, Ile892, Leu1019, Cys1024, Leu813, Ile1025, Asp1046, His1026, Arg1027, Asp1028, Gly1048, Leu1049, Lys868, Glu885		Asp814

The x-axis denotes time in ns, while the y-axis depicts RMSD values in Å for both the protein (Cα) and the ligand. Initially, from 0 to 20 ns, both the protein and ligand display relatively low RMSD values, indicating a stable conformation. The Cα RMSD remains below 2.0 Å, suggesting that the protein structure is stable during this phase. However, between 20 and 40 ns, noticeable variations occur in both RMSD curves, with the ligand exhibiting more significant fluctuations. This behavior suggests that the ligand may be adapting to its binding site or undergoing conformational changes. After approximately 40 ns, the Cα RMSD begins to increase gradually, reaching approximately 2.8 Å by the conclusion of the simulation. This increase implies that the protein undergoes conformational changes, potentially influenced by the ligand or inherent flexibility. In contrast, the ligand

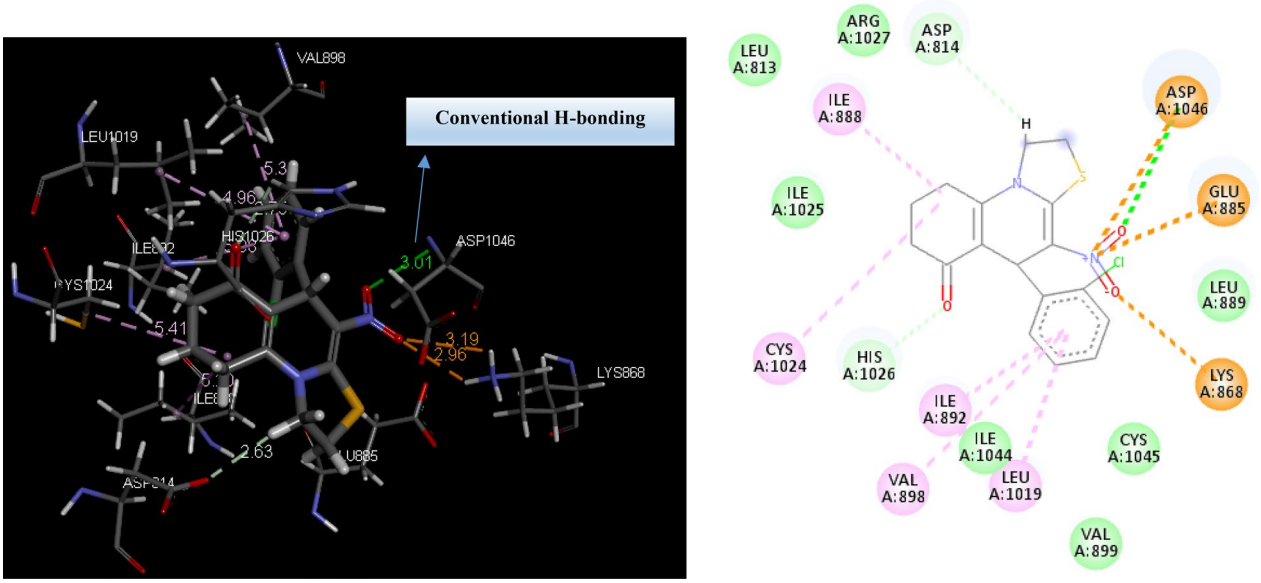

Fig. 4 The 3D and 2D binding modes of compound **(5e)** in the active site of VEGFR-2

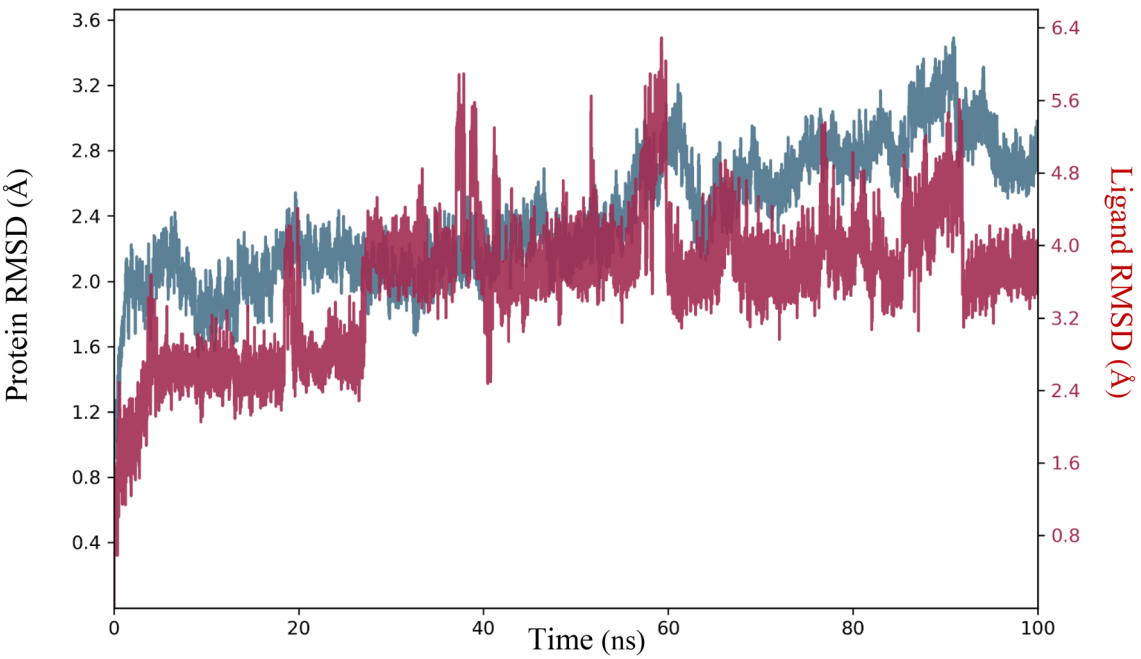

Fig. 5 RMSD plot of 100 ns MD simulations for compound **(5e)** within 2OH4

RMSD demonstrates a more pronounced increase, peaking at approximately 6.4 Å. This indicates that the ligand experiences substantial conformational changes or may be partially dissociating from the binding site during the simulation.

The RMSF (Root Mean Square Fluctuation) plot illustrates the flexibility of a protein during an MD simulation, with the x-axis representing the residue index and the y-axis indicating RMSF values in Å. As shown in Fig. 6, the RMSF values range from approximately 0.6 Å to nearly 4.8 Å, highlighting varying degrees of flexibility across different residues. Notably, residue Pro992, where the RMSF reaches approximately 4.20 Å, signifies a highly flexible region that may be involved in dynamic

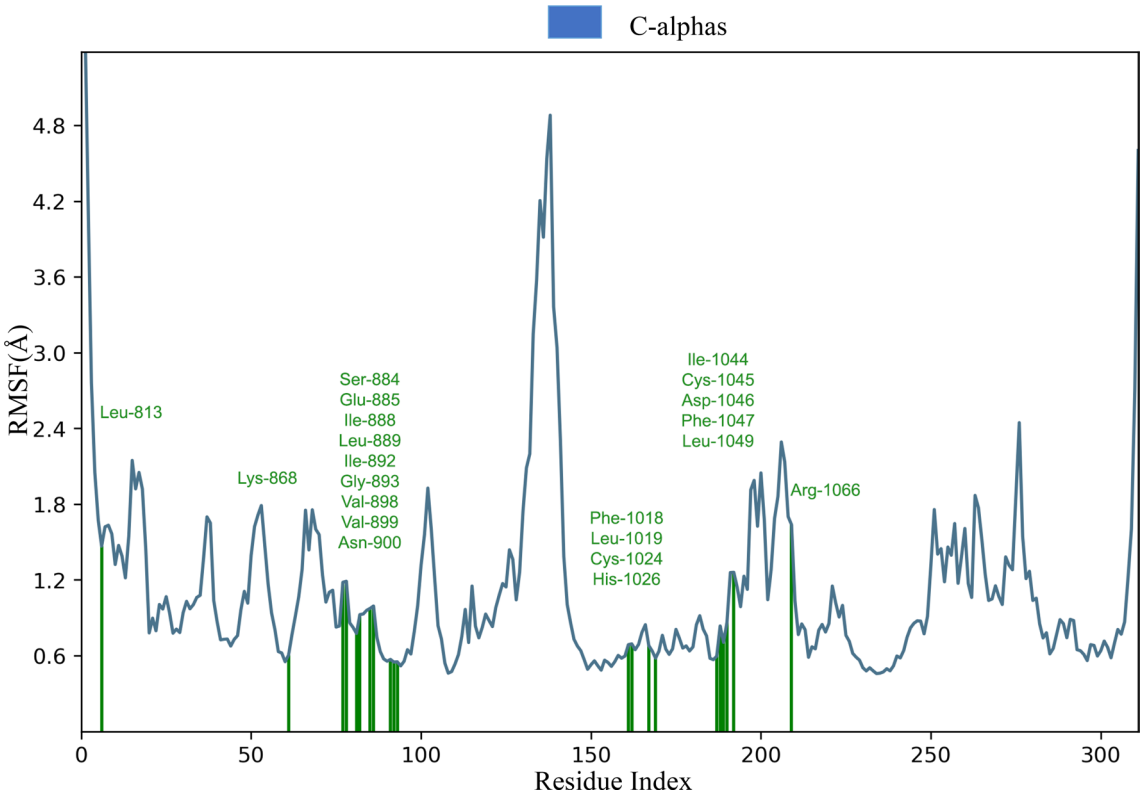

Fig.6 RMSF plot of 100 ns MD simulations for compound **(5e)** within 2OH4

processes such as ligand binding or conformational changes essential for biological function. Additional peaks around residue indices 210 and 275 also indicate significant flexibility, likely associated with loop regions or unstructured segments. In contrast, areas between the peaks, particularly around residue indices 50–80 and 280–300, exhibit relatively low RMSF values, suggesting that these regions are more rigid and stable, possibly corresponding to structured elements like alpha helices or beta sheets. The green bars in the plot highlight specific residues of interest, such as Leu813, Lys868, Ser884, Glu885, Ile888, Leu889, Ile892, Gly893, Val898, Val899, Asn900, Phe1018, Leu1019, Cys1024, His1026, Ile1044, Cys1045, Asp1046, Phe1047, Leu1049, and Arg1066, which are involved in ligand interactions or critical functional sites. Most of these residues exhibit lower RMSF values, indicating greater stability, which is crucial for maintaining the structural integrity of the protein, particularly in functional domains essential for biological activity.

The provided plot illustrates the interactions between a protein and a ligand throughout a MD simulation, categorizing these interactions into four main types: hydrogen bonds, hydrophobic contacts, ionic interactions, and water bridges. The x-axis represents the residue indices of the protein, while the y-axis indicates the fraction of interactions maintained over the simulation time. As shown in Fig. 7, residues Lys868, Glu885, and Val899 exhibit the highest interaction fractions, highlighting their significant roles in stabilizing the protein–ligand complex. Specifically, Lys868 exhibits all four types of interactions: hydrogen bonds, hydrophobic contacts, ionic interactions, and water bridges. This versatility underscores its crucial role in stabilizing the protein–ligand complex and enhancing binding affinity. Residue Glu-885 is particularly noteworthy for its involvement in ionic interactions, which are crucial for the electrostatic stabilization of the protein–ligand complex. The presence of ionic interactions can significantly enhance binding affinity, especially in the context of charged ligands. Overall, this plot underscores the complexity and diversity of protein–ligand interactions, emphasizing the importance of each interaction type in maintaining the stability and specificity of the binding process.

The examination of the entrapment of compounds within designated amino acid residues yields significant insights into the fundamental binding mechanisms. As illustrated in Fig. 8, Lys868 stands out as one of the amino acids with the highest interaction frequency throughout the simulation. Its consistent presence in the

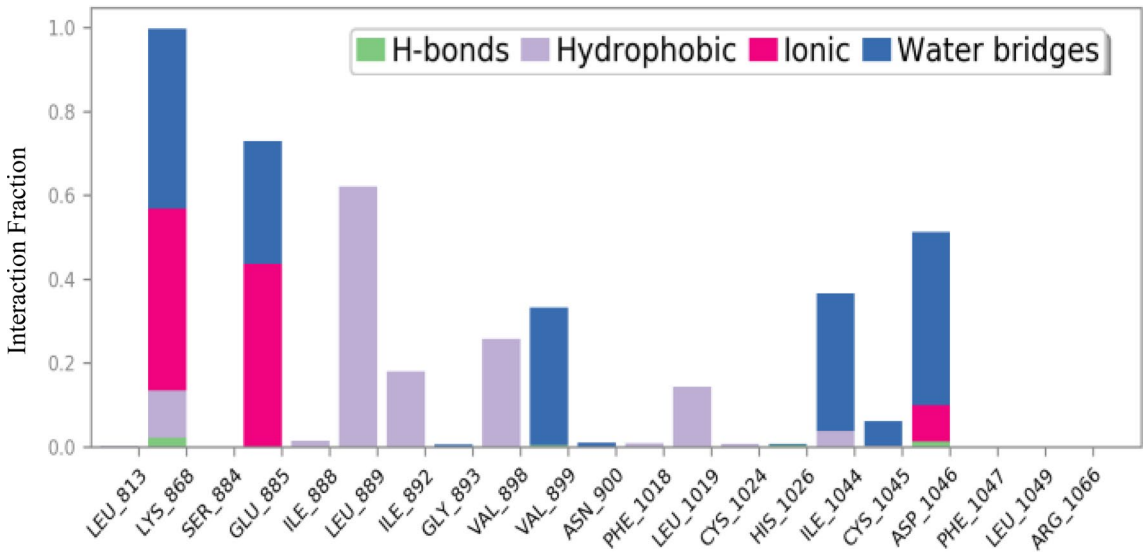

Fig. 7 The interactions of 2OH4 with compound **(5e)** throughout the simulation

contact profile indicates its crucial role in stabilizing the protein–ligand complex. This residue participates in multiple types of interactions, including hydrogen bonds and ionic interactions, which are essential for maintaining the structural integrity of the binding site. Glu885 also shows significant interaction, with numerous contact points throughout the simulation. Its involvement in ionic and water bridge interactions can enhance the electrostatic stabilization of the complex, contributing to a stronger binding affinity. Leu899 and Val898 are other notable residues that exhibit high coverage, indicating their importance in the hydrophobic interactions that help stabilize the ligand within the binding pocket. The consistent contact patterns for these residues suggest they play a vital role in the overall stability of the protein–ligand interaction. Additionally, residues such as Ile1044 and Asp1046 demonstrate significant interaction, maintaining contact for approximately 73% of the simulation time. Leu1019 also shows minimal interactions, indicating that these residues may not contribute significantly to the stabilization of the protein–ligand complex. Their limited contact with the ligand could imply that they are either less involved in the binding process or that their interactions are transient and not essential for maintaining the overall stability of the complex.

The 2D-trajectory interaction diagram provides a detailed representation of the interactions between the ligand and protein residues throughout the MD simulation. This diagram highlights interactions that occur for more than 30% of the simulation time, indicating significant contacts that may influence the ligand's binding affinity and overall stability. As shown in Fig. 9, specific protein residues that interact with the ligand are clearly identified in the diagram. For instance, LYS 868 shows a significant interaction with the ligand, occurring 43% of the time. The positive charge of LYS 868 likely facilitates ionic interactions with the negatively charged oxygen atoms on the ligand. ASP 1046 also exhibits a notable interaction, occurring 32% of the time. The negatively charged side chain of aspartate can form salt bridges with the positively charged nitrogen of the ligand, enhancing binding stability. ILE 1044 interacts with water 32% of the time, suggesting that hydrophobic interactions play a role in stabilizing the ligand–protein complex. Water molecules can mediate interactions between the ligand and protein residues, influencing the binding dynamics.

The analysis of the MD data shown in Fig. 10 reveals several important insights regarding the ligand properties over the simulation time. The RMSD plot shows fluctuations ranging from 0.0 to approximately 0.81 nm throughout the simulation. These fluctuations suggest that the ligand experiences structural changes; yet, the RMSD remains within a relatively stable range, indicating that the ligand generally maintains its structural integrity throughout the simulation. The second plot, representing the radius of gyration (rGyr), exhibits variations between approximately 3.13 and 3.31 nm. This indicates changes in the compactness of the ligand. The relatively stable values suggest that the ligand maintains a consistent overall shape, although minor fluctuations may indicate some degree of flexibility. In the third plot, concerning intramolecular hydrogen bonds (intraHB), it is clearly stated that no intramolecular hydrogen bonds are detected. This absence suggests a lack of strong intramolecular

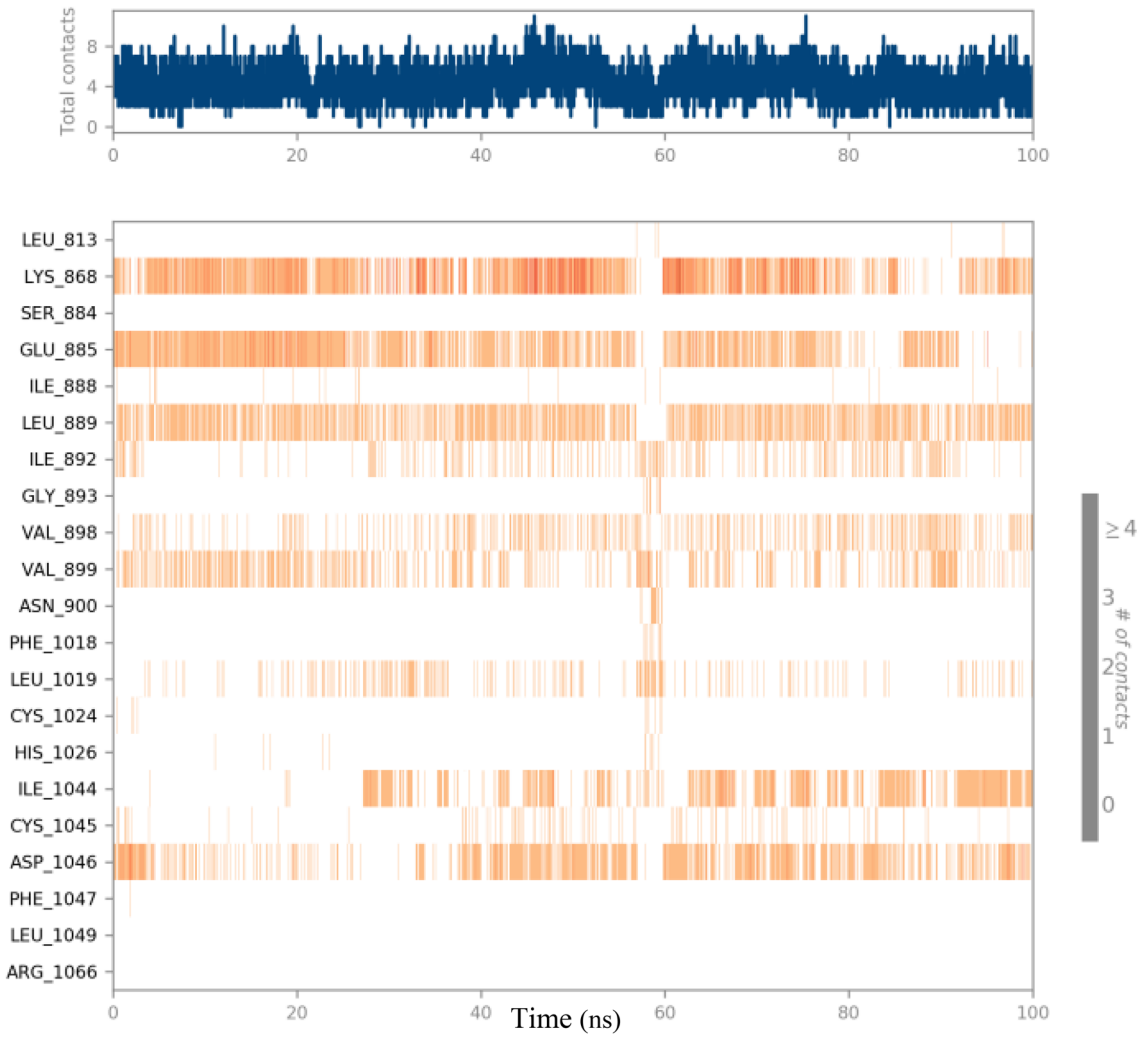

Fig. 8 Observed interaction fraction throughout the simulated trajectory

interactions, which may point to potential structural weaknesses or instability within the ligand. The fourth plot illustrates the molecular surface area (MolSA), showing fluctuations between 284 and 295 Å^2. These variations reflect changes in the ligand's exposure to the solvent environment. The relatively stable range indicates that the ligand maintains a consistent surface area throughout the simulation, suggesting that it remains accessible to the solvent. The fifth plot, depicting the solvent-accessible surface area (SASA), shows fluctuations within a similar range, indicating values between 9.22 and 96.75 Å^2. This suggests that the ligand's exposure to the solvent remains stable, with minor fluctuations indicating changes in the ligand's orientation or conformation in relation to the solvent. The sixth plot presents the polar surface area (PSA), which fluctuates between 88 and 112 Å^2. These variations indicate changes in the ligand's interactions with polar solvents. The observed fluctuations may suggest increased exposure of the ligand to polar solvents during the simulation, which could influence its solubility and interaction with the surrounding environment. Overall, the ligand appears to maintain its structural stability throughout the simulation, as indicated by the relatively stable RMSD and radius of gyration values. However, the absence of intramolecular hydrogen bonds may indicate potential structural weaknesses. The variations in SASA and PSA provide insights into the ligand's interactions with the solvent, highlighting its accessibility and potential solubility characteristics.

The torsional degree of freedom refers to the rotational movement around a single bond within a molecule, enabling the molecule to achieve an optimal conformation for interaction with proteins. In the case of the **(5e)**-2OH4 complex, the values for the torsional degrees of freedom were calculated. The trajectory simulation revealed fluctuations in specific bonds within compound

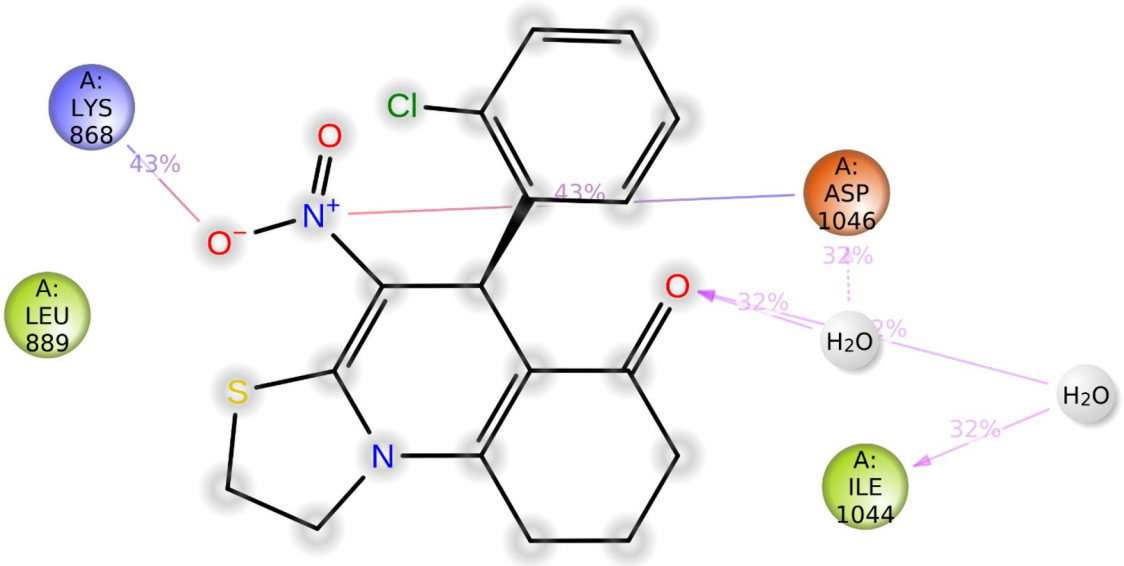

Fig. 9 Schematic diagram interactions of compound **(5e)** with 2OH4 for more than 30.0% of the simulation time

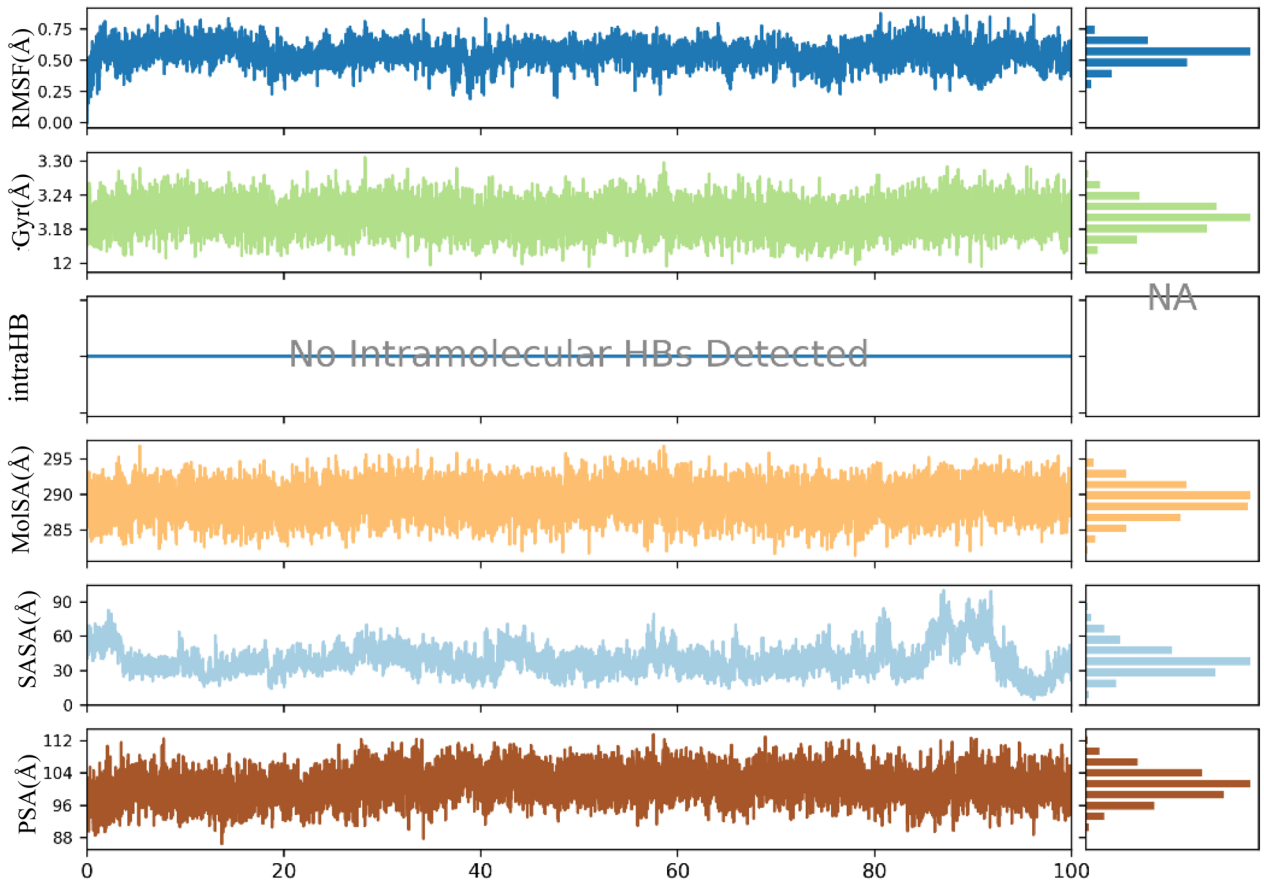

Fig. 10 Ligand properties of the **(5e)**-2OH4 complex during the 100 ns of MD Simulation

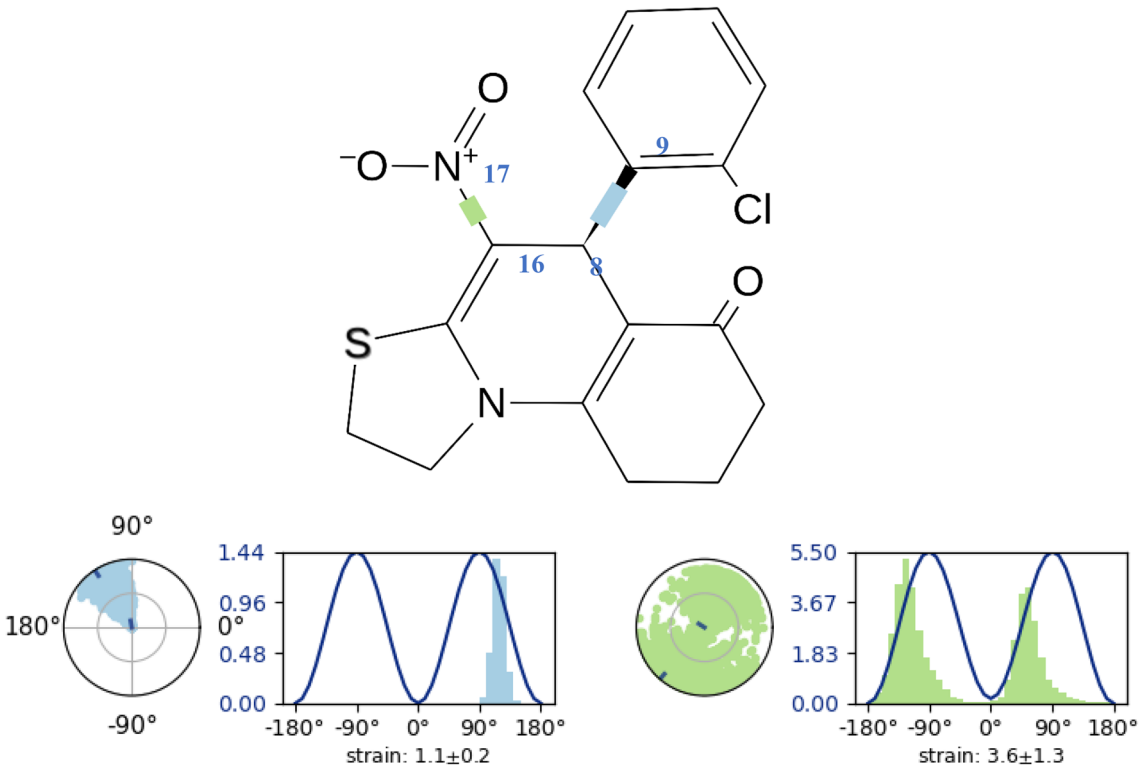

Fig. 11 The 2D schematic and torsional analysis of compound **(5e)**, illustrating the different rotatable bonds

(5e). As illustrated in Fig. 11, during the course of this simulation, both a C-N bond and a C–C bond exhibited changes in their torsional conformations. Notably, the bond between atoms 16 and 17 displayed two distinct conformations. Additionally, Fig. 11 indicates that the potential differences recorded between atoms 8 and 9, as well as between atoms 16 and 17, were measured at 1.44 and 5.50 units, respectively.

In silico drug-likeness

Drug-likeness denotes the extent to which a certain molecule mimics authorized pharmacological agents. This concept depends on achieving an ideal equilibrium of molecular and structural attributes. Assessing drug-likeness requires a comprehensive examination of several molecular parameters, including hydrophobicity, electronic distribution, hydrogen bonding capacity, molecular weight (MW), and the presence of pharmacophoric groups, bioavailability, chemical reactivity, toxicity, and metabolic stability [30]. Lipinski's Ro5 is used to assess the drug-likeness of a molecule, specifically its appropriateness for oral delivery. Lipinski asserts that an oral medication candidate must exhibit the following attributes: a MW of ≤ 500, a partition coefficient (log P) of ≤ 5, a maximum of 10 rotatable bonds, and no more than 5 HBD and 10 HBA. To be regarded as a drug contender, molecules must meet all five requirements. Ghose's law describes a drug-like molecule as having a MW between 160 and 480, a log P value between -0.4 and 5.6, a molar refractivity between 40 and 130, and an atom count between 20 and 70. According to Veber's rule, a medication with good oral bioavailability must satisfy the requirements of having no more than 10 rotatable bonds and a topological polar surface area (TPSA) ≤ 140 Å^2. Egan's parameters for optimal oral bioavailability stipulate a TPSA of ≤ 130 Å^2 and log P values ranging from -1.0 to 5.8. Ultimately, Muegge's rule enhances the criteria for identifying drug-like molecules by expanding the permissible range of attributes and integrating additional features to improve the accuracy of drug-likeness evaluations. The drug-likeness of the derivatives **(5a–l)** was assessed using the online server SwissADME [31], and the findings indicated that all of the compounds **(5a–l)** fully conformed to the five rules, with their TPSA within the range suitable for absorption. In addition, pharmaceutical chemistry has utilized pan-assay interference substances (PAINS) structural warnings to identify structural components of compounds that may cause reactivity, toxicity, or instability. There were no PAINS warnings for any of the compounds **(5a–l)**. The synthetic accessibility (SA) score was utilized to

Table 4 Pharmacokinetic properties of the compounds **(5a–l)**

Compound	MW (g/mol)	HBA	HBD	TPSA	MLog P	MR	nRot	Lipinski	Ghose	Veber's rule	Muegge	PAINS (alert)	SA score
5a	328.39	3	0	91.43	1.42	94.90	2	Yes	Yes	Yes	Yes	0	4.14
5b	358.41	4	0	100.66	1.11	101.39	3	Yes	Yes	Yes	Yes	0	4.21
5c	346.38	4	0	91.43	1.80	94.85	2	Yes	Yes	Yes	Yes	0	4.14
5d	358.41	4	0	100.66	1.11	101.39	3	Yes	Yes	Yes	Yes	0	4.23
5e	362.83	3	0	91.43	1.92	99.91	2	Yes	Yes	Yes	Yes	0	4.18
5f	374.41	5	1	120.89	0.58	103.41	3	Yes	Yes	Yes	Yes	0	4.31
5 g	362.83	3	0	91.43	1.92	99.91	2	Yes	Yes	Yes	Yes	0	4.11
5 h	362.83	3	0	91.43	1.92	99.91	2	Yes	Yes	Yes	Yes	0	4.10
5i	344.38	4	1	111.66	0.87	96.92	2	Yes	Yes	Yes	Yes	0	4.14
5j	423.28	4	1	111.66	1.49	104.62	2	Yes	Yes	Yes	Yes	0	4.22
5 k	388.44	5	0	109.89	0.81	107.88	4	Yes	Yes	Yes	Yes	0	4.37
5 l	358.41	4	0	100.66	1.11	101.39	3	Yes	Yes	Yes	Yes	0	4.25

quantify the complexity of synthesizing these drug-like molecules, providing an indicator of how feasible their synthesis would be. Table 4 demonstrates that all derivatives display favorable SA scores, indicating that these compounds can be synthesized with relative ease.

In silico ADMET prediction

ADMET prediction is a vital step in drug profiling during the drug discovery process. Table 5 provides a summary of the in *silico* ADMET parameters for compounds **(5a–l)** using the pkCSM server [32]. According to the results, all compounds demonstrated significant intestinal absorption, with compound **(5a)** having the greatest absorption rate at 95.518%. Three main distribution-related factors volume of distribution (VD), BBB permeability, and CNS permeability were assessed. The analysis revealed that all compounds exhibited satisfactory VDs, suggesting favorable systemic distribution. Nevertheless, the compounds exhibited weak permeability across the BBB and CNS, indicating limited penetration into critical CNS regions. Additionally, the compounds were evaluated for their metabolic activity against key cytochrome P450 (CYP) enzymes. The findings indicated that while all compounds were inactive against CYP2D6, CYP2C9, and CYP3A4 inhibitors, they exhibited activity as CYP3A4 substrates. These results show that the produced compounds demonstrate substantial metabolic activity within the human body, thereby helping to define their pharmacological properties. Although the pharmacokinetic properties were good, the in *silico* toxicity evaluation produced some significant results. Except for compound **(5a)**, none of the other compounds showed AMES toxicity, suggesting possible mutagenic properties for **(5a)**. Compounds **(5b)**, **(5d)**, **(5e)**, **(5f)**, **(5g)**, **(5h)**, **(5k)**, and **(5l)** were identified as hepatotoxic, indicating possible detrimental effects on hepatic cells. Although these compounds have favorable pharmacokinetic profiles, the detected toxicities raise considerable concerns. Altering the structure of these compounds could reduce toxicity concerns and improve safety. These results emphasize the essential balance between effectiveness and safety, highlighting the need for further improvements to mitigate toxicity levels.

Conclusion

Cancer is the second leading cause of mortality in approximately 112 countries. A hallmark of many cancer types is the upregulation of angiogenesis, a critical process for tumor growth. The activation of several chemical signaling pathways drives angiogenesis, which is the development of new blood vessels from pre-existing vasculature. Many cancer cells overexpress their receptors, including VEGFR-2, which plays a crucial role in the control of tumor angiogenesis. Therefore, the discovery of new agents that can be used to regulate angiogenesis is extremely important today. The FDA has approved two drugs, Pazopanib and Sorafenib, as angiogenesis inhibitors in cancer treatment, both of which possess the necessary pharmacophoric features. In light of the side effects associated with compounds such as Sorafenib and Pazopanib, researchers are actively engaged in the design of novel compounds. In this context, we have successfully designed and synthesized a novel class of thiazoloquinolinone derivatives targeting VEGFR-2, incorporating key pharmacophoric features. The synthesized compounds exhibit several important pharmacophoric characteristics that enhance their potential as drug candidates. Notably, these derivatives contain multiple heteroaromatic rings, which facilitate π–π stacking interactions with target receptors, thereby increasing

Table 5 ADMET profile of the compounds **(5a–l)**

Compound	Absorption		Distribution					Metabolism				Excretion	Toxicity	
	Intestinal absorption (human	VDss	BBB permeability	CNS permeability	Substrate		Inhibitors	2C19	2C9	2D6	3A4	Total clearance	AMES toxicity	Hepatotoxicity
					2D6	3A4	1A2							
	Numeric (% Absorbed)	Numeric (L kg − 1)	Numeric (log BB)	Numeric (log PS)				categorical (yes/no)				Numeric (mL min − 1 kg − 1)	Categorical (Yes/No)	
5a	95.518	0.231	0.014	− 1.965	No	Yes	Yes	Yes	No	No	No	0.229	Yes	No
5b	95.514	0.085	− 0.437	− 2.129	No	Yes	Yes	Yes	No	No	No	0.256	No	Yes
5c	94.759	0.06	0.006	− 2.003	No	Yes	Yes	Yes	No	No	No	0.078	No	No
5d	95.514	0.085	− 0.437	− 2.129	No	Yes	Yes	Yes	No	No	No	0.263	No	Yes
5e	93.857	0.19	0.013	− 1.85	No	Yes	Yes	Yes	No	No	No	0.161	No	Yes
5f	90.426	− 0.111	− 0.663	− 2.319	No	Yes	No	No	No	No	No	0.357	No	Yes
5 g	93.857	0.19	0.013	− 1.85	No	Yes	Yes	Yes	No	No	No	0.096	No	Yes
5 h	93.857	0.19	0.013	− 1.85	No	Yes	Yes	Yes	No	No	No	0.101	No	Yes
5i	92.633	0.038	− 0.434	− 2.154	No	Yes	No	No	No	No	No	0.109	No	No
5j	90.905	0.004	− 0.611	− 2.017	No	Yes	No	No	No	No	No	0.078	No	No
5 k	95.511	− 0.064	− 0.666	− 2.293	No	Yes	No	No	No	No	No	0.389	No	Yes
5 l	95.514	0.085	− 0.437	− 2.129	No	Yes	Yes	Yes	No	No	No	0.381	No	Yes

binding affinity. The presence of a hydroxyl group serves as a HBD, while the carbonyl and nitro groups act as HBA, further promoting interactions with the receptor. Additionally, the methoxy group and the aromatic rings contribute to the compounds' lipophilic character, enhancing hydrophobic interactions with the receptor. A central linker connects these pharmacophoric elements, providing flexibility and optimal spatial orientation for binding. Furthermore, the inclusion of sulfur groups may contribute to specific interactions, potentially enhancing the biological activity of the compounds. To investigate the potential of these compounds, we conducted computational studies, including molecular docking, MD simulations, and pharmacokinetic profiling. The docking results indicated that all synthesized compounds exhibit high binding affinities for VEGFR-2, with compound **(5e)** demonstrating the highest binding affinity, as evidenced by a docking score of − 6.63 kcal/mol. Compound **(5e)** forms a hydrogen bond with Asp1046 and the oxygen atoms of the nitro group, as well as a carbon-hydrogen bond with Asp814 and a CH2 group. The binding of compound **(5e)** is significantly influenced by hydrophobic interactions with Leu1019, Val898, Ile892, Cys1024, and Ile888. The RMSD analysis demonstrated that compound **(5e)** consistently maintained stable interactions with key residues of VEGFR-2, indicating that the **(5e)**-VEGFR-2 complex remained thermodynamically stable throughout the 100 ns trajectory. Furthermore, the analysis of ADME properties revealed that all compounds possess favorable pharmacological characteristics, and none of the compounds violate Lipinski's Rule of Five, as well as the Ghose, Veber, and Egan rules. These findings suggest that the synthesized compounds could be effective against VEGFR-2.

Experimental

General

All chemicals were purchased from Merck or Aldrich and were used without further purification. Melting points were measured on an Electrothermal 9100 apparatus. IR spectra were recorded as KBr pellets on FT-IR with Bruker Tensore 27 spectrometer NMR spectra were recorded with a Bruker DRX-300 Avance instrument (300 MHz for ^{1}H and 75.4 MHz for ^{13}C) with DMSO-d_6 as solvents. Chemical shifts are reported in parts per million (δ) downfield from an internal TMS reference. Coupling constants (*J* values) are reported in hertz (Hz), and spin multiplicities are indicated by the following symbols: s (singlet), d (doublet), t (triplet), m (multiplet). Mass spectra were recorded on an Agilent Technologies 5975C VL MSD with Tripe-Axis Detector mass spectrometer operating at an ionization potential of 70 eV.

Typical procedure for preparation of (5)

A mixture of cysteamine hydrochloride (0.113 g, 1 mmol), 1,1-bis(methylthio)-2-nitro ethylene (0.165 g, 1 mmol), 10 mL H_2O/EtOH (1:1), and piperidine (99 µL, 1 mmol) was heated under reflux in a 50-mL flask for 6 h. Upon completion of the reaction (monitored by TLC using ethyl acetate/n-hexane, 1:1), aromatic aldehyde (1 mmol), and cyclohexane-1,3-dione (0.112 g, 1 mmol) were introduced to the reaction mixture, which was then stirred under reflux for the duration specified in Table 1. Subsequently, the reaction mixture was cooled to room temperature, filtered to obtain the crude product, and the solid was washed with water/ethanol (1:1) to yield product 5 in satisfactory yield.

4-Nitro-5-phenyl-1,2,5,7,8,9-hexahydro-6H-thiazolo[3,2-*a*]quinolinone (5a): Yellow solid; Yield: 0.315 g (96%); m.p. 296–298 °C. IR (KBr) ($\bar{\upsilon}_{max}$/cm^{-1}): 1654 (C=O), 1539 and 1378 (NO_2), 1254 (C-N). ^{1}H NMR (300 MHz, DMSO-d_6): 1.75–1.84 (m, 1H, CH_2), 1.96–2.02 (m, 1H, CH_2), 2.24–2.28 (m, 2H, CH_2), 2.66–2.89 (m, 2H, CH_2), 3.39–3.43 (m, 2H, CH_2S), 4.20–4.27 (m, 1H, CH_2N), 4.44–4.50 (m, 1H, CH_2N), 5.28 (s, 1H, CH), 7.13–7.18 (m, 2H, Ar), 7.23–7.27 (m, 3H, Ar). ^{13}C NMR (75.4 MHz, DMSO-d_6): 20.3, 25.9, 28.1, 35.8, 37.2, 51.4, 116.2, 123.3, 126.6, 127.7 (2C), 128.0 (2C), 143.7, 150.5, 156.7, 194.4. *m/z* (%) = 328 (M^+, 18), 282 (13), 251 (100), 205 (20), 177 (5), 149 (10). Anal. Calcd. for $C_{17}H_{16}N_2O_3S$ (328.39): C, 62.18; H, 4.91; N, 8.53; O, 14.62; S, 9.76.

5-(4-methoxyphenyl)-4-nitro-1,2,5,7,8,9-hexahydro-6*H*-thiazolo[3,2-*a*]quinolinone (5b): Yellow solid; Yield: 0.299 g (83%); m.p. 288–290 °C. IR (KBr) ($\bar{\upsilon}_{max}$/cm^{-1}): 1621 (C=O), 1507 and 1378 (NO_2), 1245 (C-N). ^{1}H NMR (300 MHz, DMSO-d_6): 1.74–1.84 (m, 1H, CH_2), 1.97–2.00 (m, 1H, CH_2), 2.23–2.27 (m, 2H, CH_2), 2.65–2.88 (m, 2H, CH_2), 3.37–3.42 (m, 2H, CH_2S), 3.69 (s, 3H, OCH_3), 4.19–4.26 (m, 1H, CH_2N), 4.43–4.47 (m, 1H, CH_2N), 5.21 (s, 1H, CH), 6.79 (d, $^{3}J_{HH}$ = 6 Hz, 2H, Ar), 7.11 (d, $^{3}J_{HH}$ = 6 Hz, 2H, Ar). ^{13}C NMR (75.4 MHz, DMSO-d_6): 20.3, 25.8, 28.3, 35.8, 36.2, 51.4, 54.9, 113.1, 116.2, 123.2, 128.8, 135.4, 194.7, 156.3, 157.4, 194.0. *m/z* (%) = 358 (M^+, 36), 312 (37), 283 (34), 251 (100), 205 (29), 149 (14). Anal. Calcd. for $C_{18}H_{18}N_2O_4S$ (358.41): C, 60.32; H, 5.06; N, 7.82; O, 17.86; S, 8.95.

5-(4-fluorophenyl)-4-nitro-1,2,5,7,8,9-hexahydro-6*H*-thiazolo[3,2-*a*]quinolinone (5c): Yellow solid; Yield: 0.281 g (81%); m.p. 274–275 °C. IR (KBr) ($\bar{\upsilon}_{max}$/cm^{-1}): 1623 (C=O), 1503 and 1376 (NO_2), 1206 (C-N). ^{1}H NMR (300 MHz, DMSO-d_6): 1.77–1.84 (m, 1H, CH_2), 1.96–2.01 (m, 1H, CH_2), 2.24–2.28 (m, 2H, CH_2), 2.66–2.74 (m, 1H, CH_2), 2.81–2.87 (m, 1H, CH_2), 3.39–3.43 (m, 2H, CH_2S), 4.20–4.27 (m, 1H, CH_2N), 4.40–4.49 (m, 1H, CH_2N), 5.26 (s, 1H, CH), 7.06 (t, $^{3}J_{HH}$ = 6 Hz, 2H, Ar), 7.24–7.28 (m, 2H, Ar). ^{13}C NMR (75.4 MHz, DMSO-d_6):

20.0 and 25.9 ($2CH_2$), 28.1 (CH_2S), 35.7 (**C**H_2CO), 36.6 (CH), 51.4 (CH_2N), 114.7 (*d*, $^2J_{CF}$ = 15.8 Hz), 116.0 (=C–NO_2), 123.2, 129.7 (*d*, $^3J_{CF}$ = 6.8 Hz), 139.9 (*d*, $^4J_{CF}$ = 2.2 Hz), 150.7 (C=**C**–S), 157.0 (**C**=C–CO), 160.8 (*d*, $^1J_{CF}$ = 181.7 Hz), 194.5 (C = O). ^{13}F NMR (471 MHz): -116.0 ppm.

5-(3-methoxyphenyl)-4-nitro-1,2,5,7,8,9-hexahydro-*6H*-thiazolo[3,2-*a*]quinolinone (5d): White solid; Yield: 0.287 g (80%); m.p. 196–198 °C. IR (KBr) ($\bar{\upsilon}_{max}$/cm^{-1}): 1627 (C=O), 1548 and 1375 (NO_2), 1224 (C–N). ^{1}H NMR (300 MHz, DMSO-D6): 1.64–1.71 (m, 1H, CH_2), 1.84–1.90 (m, 1H, CH_2), 2.13–2.17 (m, 2H, CH_2), 2.53–2.63 (m, 1H, CH_2), 2.72–2.79 (m, 1H, CH_2), 3.30–3.32 (m, 2H, CH_2S), 4.06–4.16 (m, 1H, CH_2N), 4.32–4.40 (m, 1H, CH_2N), 5.15 (s, 1H, CH), 6.62–6.69 (m, 3H, Ar), 7.05 (t, $^3J_{HH}$ = 9 Hz, 1H, Ar). ^{13}C NMR (75.4 MHz, DMSO-d_6): 20.7, 26.4, 28.6, 36.3, 37.4, 51.9, 55.3, 111,6, 114.7, 116.5, 120.4, 123.5, 129.6, 145.5, 151.3, 157.5, 159.4, 196.1.

5-(2-chlorophenyl)-4-nitro-1,2,5,7,8,9-hexahydro-*6H*-thiazolo[3,2-*a*]quinolinone (5e): Yellow solid; Yield: 0.271 g (74%); m.p. 217–218 °C. IR (KBr) ($\bar{\upsilon}_{max}$/cm^{-1}): 1706 (C=O), 1530 and 1341 (NO_2), 1261 (C–N). ^{1}H NMR (300 MHz, DMSO-d_6): 1.31–1.44 (m, 1H, CH_2), 1.75–1.79 (m, 1H, CH_2), 1.99–2.23 (m, 2H, CH_2), 2.40–2.54 (m, 1H, CH_2), 2.92–3.02 (m, 1H, CH_2), 3.10–3.3.15 (m, 2H, CH_2S), 3.15–3.61 (m, 1H, CH_2N), 3.89 (t, $^3J_{HH}$ = 9 Hz 1H, CH_2N), 5.06 (s, 1H, CH), 6.29 (s, 1H, Ar), 6.87 (t, $^3d_{HH}$ = 12 Hz, 1H, Ar), 6.99–7.09 (m, 2H, Ar), 7.26 (d, $^3J_{HH}$ = 6 Hz, 1H, Ar). ^{13}C NMR (75.4 MHz, DMSO-d_6): 20.1, 27.2, 34.8, 36.7, 49.9, 58.5, 86.9, 118.8, 126.6, 128.0, 129.4, 130.4, 132.4, 139.7, 166.0, 206.2.

5-(2-hydroxy-3-methoxyphenyl)-4-nitro-1,2,5,7,8,9-hexahydro-*6H*-thiazolo[3,2-*a*]quinolinone (5f): Yellow solid; Yield: 0.337 g (90%); m.p. 280–282 °C. IR (KBr) ($\bar{\upsilon}_{max}$/cm^{-1}): 3434 (OH), 1614 (C=O), 1532 and 1386 (NO_2), 1221 (C–N). ^{1}H NMR (300 MHz, DMSO-d_6): 1.60–1.67 (m, 1H, CH_2), 1.81–1.89 (m, 1H, CH_2), 2.11–2.16 (m, 2H, CH_2), 2.57–2.64 (m, 2H, CH_2), 3.26–3.32 (m, 2H, CH_2S), 3.61 (s, 3H, OCH_3), 4.14–4.30 (m, 2H, CH_2N), 5.18 (s, 1H, CH), 6.50–6.65 (m, 3H, Ar), 8.46 (s, 1H, OH). ^{13}C NMR (75.4 MHz, DMSO-d_6): 20.7, 26.5, 28.5, 34.9, 36.2, 51,6, 55.9, 110.4, 115.3, 118.6, 122.9, 123.2, 129.9, 145.1, 148.5, 151.6, 155.5, 195.9.

5-(4-chlorophenyl)-4-nitro-1,2,5,7,8,9-hexahydro-*6H*-thiazolo[3,2-*a*]quinolinone (5g): Yellow solid; Yield: 0.279 g (77%); m.p. 286–288 °C. IR (KBr) ($\bar{\upsilon}_{max}$/cm^{-1}): 1644 (C = O), 1534 and 1375 (NO_2), 1208 (C–N). ^{1}H NMR (300 MHz, DMSO-d_6): 1.63–1.75 (m, 1H, CH_2), 1.84–1.91 (m, 1H, CH_2), 2.12–2.17 (m, 2H, CH_2), 2.53–2.64 (m, 1H, CH_2), 2.69–2.78 (m, 1H, CH_2), 3.17–3.33 (m, 2H, CH_2S), 4.08–4.17 (m, 1H, CH_2N), 4.31–4.39 (m, 1H, CH_2N), 5.13 (s, 1H, CH), 7.17 (m, 4H, Ar). ^{13}C NMR (75.4 MHz, DMSO-d_6): 20.7, 26.4, 28.6, 36.2, 37.4, 51.9, 116.3, 123.4, 128.4, 130.2, 131.6, 143.1, 151.4, 157.6, 194.9.

5-(3-chlorophenyl)-4-nitro-1,2,5,7,8,9-hexahydro-*6H*-thiazolo[3,2-*a*]quinolinone (5h): Yellow solid; Yield: 0.285 g (82%); m.p. 253–255 °C. IR (KBr) ($\bar{\upsilon}_{max}$/cm^{-1}): 1629 (C=O), 1550 and 1375 (NO_2), 1224 (C–N). ^{1}H NMR (300 MHz, DMSO-d_6): 1.66–1.70 (m, 1H, CH_2), 1.86–1.90 (m, 1H, CH_2), 2.13–2.15 (m, 2H, CH_2), 2.55–2.61 (m, 1H, CH_2), 2.72–2.78 (m, 1H, CH_2), 3.28–3.34 (m, 2H, CH_2S), 4.08–4.17 (m, 1H, CH_2N), 4.33–4.41 (m, 1H, CH_2N), 5.14 (s, 1H, CH), 6.07–7.21 (m, 3H, Ar). ^{13}C NMR (75.4 MHz, DMSO-d_6): 20.7, 26.4, 28.6, 36.2, 37.9, 51,9, 116.1, 123.1, 127.0, 127.1, 128.2, 130.5, 133.1, 146.4, 151,6, 157.8, 195.0.

5-(4-hydroxyphenyl)-4-nitro-1,2,5,7,8,9-hexahydro-*6H*-thiazolo[3,2-*a*]quinolinone (5i): Yellow solid; Yield: 0.307 g (89%); m.p. 278–280 °C. IR (KBr) ($\bar{\upsilon}_{max}$/cm^{-1}): 1618 (C=O), 1510 and 1380 (NO_2), 1223 (C–N). ^{1}H NMR (300 MHz, DMSO-d_6): 1.73–1.84 (m, 1H, CH_2), 1.96–2.01 (m, 1H, CH_2), 2.23–2.27 (m, 2H, CH_2), 2.65–2.73 (m, 1H, CH_2), 2.80–2.87 (m, 1H, CH_2), 3.39–3.41 (m, 2H, CH_2S), 4.18–4.25 (m, 1H, CH_2N), 4.42–4.48 (m, 1H, CH_2N), 5.17 (s, 1H, CH), 6.61 (d, $^3J_{HH}$ = 9 Hz, 2H, Ar), 7.01 (d, $^3J_{HH}$ = 9 Hz, 2H, Ar), 9.25 (s, 1H, OH). ^{13}C NMR (75.4 MHz, DMSO-d_6): 20.3, 25.8, 28.1, 35.8, 36.1, 51.3, 114.7 (2C), 116.5, 123.7, 128.7 (2C), 134.3, 150.2, 155.9, 156.4, 194.5. *m/z* (%) = 344 (M^+, 34), 327 (22), 298 (30), 269 (26), 251 (100), 205 (26), 149 (16). Anal. Calcd. for $C_{17}H_{16}N_2O_4S$ (344.39): C, 59.29; H, 4.68; N, 8.13; O, 18.58; S, 9.31.

5-(5-bromo-2-hydroxyphenyl)-4-nitro-1,2,5,7,8,9-hexahydro-*6H*-thiazolo[3,2-*a*]quinolinone (5j): Yellow solid; Yield: 0.325 g (76%); m.p. 254–256 °C. IR (KBr) ($\bar{\upsilon}_{max}$/cm^{-1}): 1620 (C=O), 1531 and 1382 (NO_2), 1224 (C–N). ^{1}H NMR (300 MHz, DMSO-d_6): 1.61–1.68 (m, 1H, CH_2), 1.85–1.90 (m, 1H, CH_2), 2.11–2.14 (m, 2H, CH_2), 2.54–2.6370 (m, 2H, CH_2), 3.29–3.33 (m, 2H, CH_2S), 4.11–4.31 (m, 2H, CH_2N), 5.09 (s, 1H, CH), 6.54 (d, $^3J_{HH}$ = 9 Hz, 1H, Ar), 7.02 (d, $^3J_{HH}$ = 6 Hz, 1H, Ar), 7.14 (d, $^3J_{HH}$ = 6 Hz, 1H, Ar), 9.58 (s, 1H, OH). ^{13}C NMR (75.4 MHz, DMSO-d_6): 20.7, 26.5, 28.5, 37.3, 51.7, 110.1, 114.4, 118.7, 122.1, 130.6, 130.9, 134.2, 151.6, 155.7, 158.1, 195.5.

5-(3,4-dimethoxyphenyl)-4-nitro-1,2,5,7,8,9-hexahydro-*6H*-thiazolo[3,2-*a*]quinolinone (5k): Yellow solid; Yield: 0.311 g (80%); m.p. 218–220 °C. IR (KBr) ($\bar{\upsilon}_{max}$/cm^{-1}): 1623 (C=O), 1511 and 1373 (NO_2), 1225 (C–N). ^{1}H NMR (300 MHz, DMSO-d_6): 1.76–1.83 (m, 1H, CH_2), 1.97–2.03 (m, 1H, CH_2), 2.25–2.29 (m, 2H, CH_2), 2.66–2.74 (m, 1H, CH_2), 2.82–2.89 (m, 1H, CH_2), 3.38–3.43 (m, 2H, CH_2S), 3.69 (s, 3H, OCH_3), 3.71 (s, 3H, OCH_3), 4.19–4.26 (m, 1H, CH_2N), 4.43–4.49 (m,

1H, CH_2N), 5.24 (s, 1H, CH), 6.65 (d, $^3J_{HH}$ = 9 Hz, 1H, Ar), 6.81 (d, $^3J_{HH}$ = 9 Hz, 2H, Ar). ^{13}C NMR (75.4 MHz, DMSO-d_6): 20.3, 25.8, 28.2, 35.8, 36.3, 51.4, 55.4, 111.6, 111.9, 116.3, 119.2, 123.4, 136.3, 147.5, 148.2, 150.5, 156.6, 194.6. m/z (%) = 388 (M^+, 32), 371 (40), 342 (25), 313 (46), 251 (100), 205 (26), 149 (13). Anal. Calcd. for $C_{19}H_{20}N_2O_5S$ (388.44): C, 58.75; H, 5.19; N, 7.21; O, 20.59; S, 8.25.

5-(2-methoxyphenyl)-4-nitro-1,2,5,7,8,9-hexahydro-*6H*-thiazolo[3,2-*a*]quinolinone (5i): Yellow solid; Yield: 0.273 g (76%); m.p. 196–198 °C. IR (KBr) ($\tilde{\upsilon}_{max}$/cm^{-1}): 1627 (C=O), 1547 and 1375 (NO_2), 1224 (C–N). ^{1}H NMR (300 MHz, DMSO-d_6): 1.62–1.74 (m, 1H, CH_2), 1.84–1.92 (m, 1H, CH_2), 2.13–2.18 (m, 2H, CH_2), 2.53–2.63 (m, 1H, CH_2), 2.70–2.79 (m, 1H, CH_2), 3.27–3.32 (m, 2H, CH_2S), 3.59 (s, 3H, OCH_3), 4.06–4.16 (m, 1H, CH_2N), 4.32–4.40 (m, 1H, CH_2N), 5.15 (s, 1H, CH), 6.62–6.68 (m, 3H, Ar), 7.05 (t, $^3J_{HH}$ = 9 Hz, 1H, Ar). ^{13}C NMR (75.4 MHz, DMSO-d_6): 20.7, 26.4, 28.6, 36.3, 37.2, 51.8, 55.3, 111.6, 114.7, 116.5, 120.3, 123.5, 129.6, 145.5, 151.3, 157.5, 159.4, 195.0.

Computational studies

Molecular docking studies

The crystallographic structures of VEGFR-2 (PDB ID: 2OH4) were obtained from the RCSB Protein Data Bank. All preparations for protein docking were carried out using the Protein Preparation Wizard [33], which involved optimizing the protein structure and addressing any missing residues. The OPLS_2005 force field was employed to prepare the synthesized derivatives at a physiological pH of 7.0 ± 2 [34]. Molecular docking simulations were conducted using Schrödinger software [35], specifically utilizing the Glide module with standard accuracy and flexible ligand sampling. This approach generated grid boxes of 26 Å at each binding site and reported ten poses for each ligand. The two-dimensional (2D) and three-dimensional (3D) interactions were visualized using BIOVIA Discovery Studio [36].

MD simulations

MD simulations were conducted using Desmond software through the Schrödinger Maestro interface [37]. The results obtained from the MD simulations were consistent with those derived from the previous docking studies involving the complex. The simulation cell was configured as orthorhombic and was filled with water molecules according to the SPC (Simple Point Charge) model. Additionally, sufficient ions were added to neutralize the overall charge of the complex. The simulation duration was set to 100 ns, operating under the NPT (constant Number of particles, Pressure, and Temperature) ensemble framework. Throughout the simulation, the number of atoms remained constant, with pressure maintained at 1.01325 bar and temperature at 300 K. The default thermostat utilized was the Nose–Hoover chain method, with a coupling time constant of 1.0 picosecond, while the Martyna-Tobias-Klein method was employed as the default barostat, set to a coupling time constant of 2.0 picoseconds. The MD simulation results were analyzed using the Maestro simulation interaction diagram.

Evaluation of drug-likeness and in silico ADMET prediction

The methodology employed for assessing the drug-likeness and pharmacokinetic profiles of the synthesized thiazoloquinolinone derivatives **(5a–l)** involved the use of the SwissADME online platform. This approach facilitated the evaluation of several established drug-likeness criteria, including Lipinski's Ro5, Veber's Rule, Ghose's Rule, and Egan's Rule. These criteria were meticulously applied to ascertain the drug-likeness profiles of the synthesized derivatives. Additionally, in *silico* ADMET predictions were performed using the pkCSM platform to analyze the pharmacokinetic properties of the compounds. This comprehensive strategy provided valuable insights into the pharmacokinetic characteristics of the derivatives and their potential as promising drug candidates.

Supplementary Information

The online version contains supplementary material available at https://doi.org/10.1186/s13065-025-01459-5.

Supplementary Material 1.

Acknowledgements
Not applicable.

Author contributions
This paper has three authors, and our individual contributions were as below: Contributions by Authors Zeinab Amiri: participated in the design of the study, and drafted the manuscript. Mohammad Bayat: conceived of the study, carried out the literature survey, participated in the design of the study, and drafted the manuscript. Davood Gheidari: conceived of the study, carried out the literature survey, participated in the design of the study, and drafted the manuscript.

Funding
The authors declare that no funds, grants, or other support were received during the preparation of this manuscript.

Data availability
All data generated or analyzed during this study are included in this published article and its supplementary information files.

Declarations

Ethics approval and consent to participate
Not applicable.

Consent for publication
Not applicable.

Competing interests
The authors declare no competing interests.

Received: 21 December 2024 Accepted: 18 March 2025
Published online: 05 April 2025

References

1. Sung H, Ferlay J, Siegel RL, Laversanne M, Soerjomataram I, Jemal A, Bray F. Global cancer statistics 2020: GLOBOCAN estimates of incidence and mortality worldwide for 36 cancers in 185 countries. CA Cancer J Clin. 2021;71:209–49.
2. Zhong L, Li Y, Xiong L, Wang W, Wu M, Yuan T, Yang W, Tian C, Miao Z, Wang T, Yang S. Small molecules in targeted cancer therapy: advances, challenges, and future perspectives. Sig Transduct Target Ther. 2021;6:201.
3. Liu Z-L, Chen H-H, Zheng L-L, Sun L-P, Shi L. Angiogenic signaling pathways and anti-angiogenic therapy for cancer. Sig Transduct Target Ther. 2023;8:198.
4. Sana S, Reddy VG, Bhandari S, Reddy TS, Tokala R, Sakla AP, Bhargava SK, Shankaraiah N. Exploration of carbamide derived pyrimidine-thioindole conjugates as potential VEGFR-2 inhibitors with anti-angiogenesis effect. Eur J Med Chem. 2020;200: 112457.
5. Lee K, Jeong K-W, Lee Y, et al. Pharmacophore modeling and virtual screening studies for new VEGFR-2 kinase inhibitors. Eur J Med Chem. 2010;45:5420–7.
6. Machado VA, Peixoto D, Costa R, et al. Synthesis, antiangiogenesis evaluation, and molecular docking studies of 1-aryl-3-[(thieno[3,2-b]pyridin-7-ylthio)phenyl]ureas: discovery of a new substitution pattern for type II VEGFR-2 Tyr kinase inhibitors. Bioorg Med Chem. 2015;23:6497–509.
7. Dietrich J, Hulme C, Hurley LH. The design, synthesis, and evaluation of 8 hybrid DFG-out allosteric kinase inhibitors: a structural analysis of the binding interactions of Gleevec. J Med Chem. 2010;53:1234–45.
8. Wu P, Nielsen TE, Clausen MH. FDA-approved small-molecule kinase inhibitors. Trends Pharmacol Sci. 2015;36:422–39.
9. Abdallah AE, Mabrouk RR, Elnagar MR, Farrag AM, Kalaba MH, Sharaf MH, El-Fakharany EM, Bakhotmah DA, Elkaeed EB, AlWard MMS. New series of VEGFR-2 inhibitors and apoptosis enhancers: design, synthesis and biological evaluation. Drug Des Dev Ther. 2022;16:587–606.
10. Kankanala J, Latham A, Johnson A, Homer-Vanniasinkam S, Fishwick C, Ponnambalam S. A combinatorial in silico and cellular approach to identify a new class of compounds that target VEGFR2 receptor tyrosine kinase activity and angiogenesis. Br J Pharmacol. 2012;166:737–48.
11. Boudou-Rouquette P, Bensalah K, Ravaud A, Gauthier M, Giraud A, Goudet P, Guillemin F, Giraud P, Giraud M, et al. Clinical pharmacology, drug–drug interactions, and safety of pazopanib: a review. Expert Opin Drug Metab Toxicol. 2016;12:1433–44.
12. Arshad MF, Alam A, Alshammari AA, Alhazza MB, Alzimam IM, Alam MA, Mustafa G, Ansari MS, Alotaibi AM, Alotaibi AA, et al. Thiazole: a versatile standalone moiety contributing to the development of various drugs and biologically active agents. Molecules. 2022;27:3994.
13. Raveesha R, Anusuya AM, Raghu AV, Kumar KY, Kumar MGD, Prasad SBB, Prashanth MK. Synthesis and characterization of novel thiazole derivatives as potential anticancer agents: molecular docking and DFT studies. Comput Toxicol. 2022;21: 100202.
14. Litim B, Djahoudi A, Meliani S, Boukhari A. Synthesis and potential antimicrobial activity of novel aminophosphonates derivatives bearing substituted quinoline or quinolone and thiazole moieties. Med Chem Res. 2022;31:60–74.
15. Abdel-Aziz SA, Taher ES, Lan P, El-Koussi NA, Salem OIA, Gomaa HAM, Youssif BGM. New pyrimidine/thiazole hybrids endowed with analgesic, anti-inflammatory, and lower cardiotoxic activities: design, synthesis, and COX-2/sEH dual inhibition. Arch Pharm. 2022;355: e2200024.
16. El-Hazek RMM, Zaher NH, El-Gazzar MGM, El-Sayed MA, El-Shafey A, El-Masry A, El-Sayed MA. Novel VEGFR2 inhibitors with thiazoloquinoxaline scaffold targeting hepatocellular carcinoma with lower cardiotoxic impact. Sci Rep. 2023;13:13907.
17. Tokalı FS, Şenol H, Yetke Hİ, Hacıosmanoğlu-Aldoğan E. Novel quinazoline–chromene hybrids as anticancer agents: synthesis, biological activity, molecular docking, dynamics and ADME studies. Arch Pharm. 2023;356(11):2300423.
18. Altıntop MD, Sever B, Çiftçi GA, Özdemir A. Design, synthesis, and evaluation of a new series of thiazole-based anticancer agents as potent Akt inhibitors. Molecules. 2018;23:1318.
19. Hassan A, Badr M, Hassan HA, Abdelhamid D, Abuo-Rahma GEDA. Novel 4-(piperazin-1-yl)quinolin-2(1*H*)-one bearing thiazoles with antiproliferative activity through VEGFR-2-TK inhibition. Bioorg Med Chem. 2021;40: 116168.
20. El-Naggar AM, Zidan A, Elkaeed EB, Taghour MS, Badawi WA. Design, synthesis and docking studies of new hydrazinylthiazole derivatives as anticancer and antimicrobial agents. J Saudi Chem Soc. 2022;26: 101488.
21. Çakır F, Atesoğlu Ş, Kose A, Ghaffari-Moghaddam M, Akbaş F, Kınay H, Kuran ED, Ulusoy-Güzeldemirci N, Kılınç N, Tokalı FS, Şenol H. Novel 4-((3-fluorobenzyl)oxy)benzohydrazide derivatives as promising anti-prostate cancer agents: synthesis, characterization, and in vitro & in silico biological activity studies. J Mol Struct. 2025;1322: 140702.
22. Gheidari D, Mehrdad M, Bayat M. Synthesis, molecular docking, molecular dynamics simulation, ADMET, drug likeness, and DFT studies of novel Furo[2,3-b]indol-3a-ol as promising cyclin-dependent kinase 2 inhibitors. Sci Rep. 2024;14:3084.
23. Gheidari D, Mehrdad M, Bayat M. Novel indenopyrrol-4-one derivatives as potent BRDT inhibitors: Synthesis, molecular docking, drug-likeness, ADMET, and DFT studies. J Biomol Struct Dyn. 2024;42:7860–73.
24. Gheidari D, Mehrdad M, Bayat M. Synthesis, molecular docking analysis, molecular dynamics simulation, ADMET, DFT, and drug likeness studies: novel Indeno[1,2-b]pyrrol-4(1H)-one as SARS-CoV-2 main protease inhibitors. PLoS ONE. 2024;19(3): e0299301.
25. Mahmoodi N, Bayat M, Gheidari D, Sadeghian Z. In silico evaluation of cis-dihydroxy-indeno[1,2-d]imidazolones as inhibitors of glycogen synthase kinase-3: synthesis, molecular docking, physicochemical data, ADMET, MD simulation, and DFT calculations. J Saudi Chem Soc. 2024;28(4): 101894.
26. Aghahosseinia F, Bayat M, Sadeghiana Z, Gheidari D, Safari F. Synthesis, molecular docking study, MD simulation, ADMET, and drug likeness of new thiazolo[3,2-a]pyridine-6,8-dicarbonitrile derivatives as potential anti-diabetic agents. PLoS ONE. 2024;19: e0306973.
27. Bayat M, Hosseini F, Nasri S. An efficient one-pot synthesis of tetrahydrothiazolo[3,2-*a*]quinolin-6-one derivatives. J Sulfur Chem. 2018;39(1):99–111.
28. RCSB Protein Data Bank. Retrieved from https://www.rcsb.org.
29. Gheidari D, Mehrdad M, Hosseini F. Virtual screening, molecular docking, MD simulation studies, DFT calculations, ADMET, and drug likeness of diaza-adamantane as potential MAPK/ERK inhibitors. Front Pharmacol. 2024;15:1360226.
30. Gheidari D, Mehrdad M, Karimelahi Z. Virtual screening, ADMET prediction, molecular docking, and dynamic simulation studies of natural products as BACE1 inhibitors for the management of Alzheimer's disease. Sci Rep. 2024;14:26431.
31. Daina A, Michielin O, Zoete V. SwissADME: A free web tool to evaluate pharmacokinetics, drug-likeness, and medicinal chemistry friendliness of small molecules. Sci Rep. 2017;7:42717.
32. Pires DEV, Blundell TL, Ascher DB. Predicting small-molecule pharmacokinetic and toxicity properties using graph-based signatures. J Med Chem. 2015;58(9):4066–72.
33. Schrödinger E. Protein preparation wizard. In: Schrödinger Suite 2017-1; Schrödinger, LLC: New York, 2017.
34. Schrödinger E. LigPrep. In: Schrödinger Release 2017-1; Schrödinger, LLC: New York, 2017.
35. Schrödinger E. The Schrödinger Suite 2017-1; Schrödinger, LLC: New York, NY, 2017.
36. Dassault Systèmes. BIOVIA Discovery Studio Visualizer; San Diego, 2020.

37. Schrödinger E. Desmond. In: Schrödinger Release 2017-1; Schrödinger, LLC: New York, 2017.

Publisher's Note